Modular DNA Barcoding of Nanobodies Enables Multiplexed *in situ* Protein Imaging and High-throughput Biomolecule Detection

Shilin Zhong[1,2,3], Ruiyu Wang[1,2,3,4], Xinwei Gao[4], Qingchun Guo[4,5], Rui Lin[2,6,#], Minmin Luo[4,7,8,9,#]

[1]School of Life Sciences, Peking University, Beijing 100871, China.

[2]National Institute of Biological Sciences (NIBS), Beijing 102206, China.

[3]Peking University-Tsinghua University-National Institute of Biological Sciences Joint Graduate Program, NIBS, Beijing 102206, China.

[4]Chinese Institute for Brain Research, Beijing 102206, China.

[5]Capital Medical University, Beijing 100069, China.

[6]Tsinghua Institute of Multidisciplinary Biomedical Research (TIMBR), Beijing 102206, China.

[7]New Cornerstone Science Laboratory, Shenzhen 518054, China.

[8]Research Unit of Medical Neurobiology, Chinese Academy of Medical Sciences, Beijing 100005, China.

[9]Beijing Institute for Brain Research, Chinese Academy of Medical Sciences & Peking Union Medical College, Beijing, 102206, China

[#]Correspondence email: linrui@nibs.ac.cn; luominmin@cibr.ac.cn

Abstract

Immunodetection methods based on antibody-antigen interactions are routinely used in biological and clinical laboratories. DNA-labeled antibodies offer the advantage of simultaneous detection of multiple target molecules via orthogonal DNA barcode sequences. However, current methods for antibody-DNA conjugation typically involve non-site-specific modifications tailored for each specific application, a process that is labor-intensive and often compromises antibody affinity and specificity. To overcome these limitations, here we present a modular, site-specific, and cost-efficient DNA tagging strategy — multiplexed and modular barcoding of antibodies (MaMBA). Utilizing nanobodies as modular adaptors, MaMBA enables direct site-specific labeling of off-the-shelf IgG antibodies with a one-component design. We first applied MaMBA to develop the *mis*HCR method for highly multiplexed *in situ* protein imaging via orthogonal hybridization chain reaction (HCR). We then introduced a cleavable version of MaMBA, which allows iterative use of the same HCR probes sets, thereby enhancing the multiplexity of *mis*HCR (*mis*HCR^{n}). *mis*HCR^{n} achieves simultaneous labeling of 12 different target molecules within the same mouse brain sections. We further extended the cleavable MaMBA to develop the barcode-linked immunosorbent assay (BLISA) for multiplexed and high-throughput biomolecule detections. By combining BLISA with next-generation sequencing, we successfully measured SARS-CoV-2 IgG and HBV-associated antigens in a large number of human serum samples. Additionally, we demonstrated a small-scale drug screen by using BLISA to simultaneously detect eight protein targets. In conclusion, MaMBA offers a highly modular and easily adaptable approach for antibody DNA-barcoding, which can be broadly applied in basic research and clinical diagnostics.

Introduction

Accurate detection of target molecules in biological samples is key for biomedical research and clinical diagnostics. Owing to their ease of use, speed, and accessibility, immunodetections are currently the standard and most popular methods for biomolecule detection[1,2]. These methods use a primary antibody that binds selectively to a target molecule (antigen). This primary antibody-antigen interaction can be visualized via a conjugated reporter (*e.g.*, horseradish peroxidase or fluorophore) on the antibody. In most cases, a labeled secondary antibody, which can recognize the primary antibodies from the same host species, reacts with the antibody-antigen complex to generate readout signals. In classic immunodetection methods, chromogen, fluorescence, or luminescence is utilized to optically report the abundance and localization of target molecules. However, the overlaps of antibody species and reporter spectrums limit the simultaneous detection of only a few (often up to three) target molecules in a sample[3].

DNA barcoding represents a promising strategy to improve the multiplexity and efficiency of conventional immunodetection methods. This technique involves conjugating antibodies with DNA molecules containing unique barcode sequences, rather than traditional optical reporters. By utilizing a combination of DNA-labeled antibodies, multiple target molecules can be simultaneously detected within a single sample[4,5]. Each antibody-antigen interaction can be examined via distinct barcode sequences. Considering the high diversity of DNA sequences, DNA barcoding offers much higher multiplexity far beyond the scope of conventional reporter molecules. Importantly, careful design of DNA barcode sequences also enables pooled analyses using advanced DNA sequencing techniques, leveraging massively parallel sequencing capabilities to dramatically increase the detection throughput at low cost[6–8].

However, the process of conjugating DNA oligonucleotides to individual primary antibodies is both labor-intensive and expensive, which severely limits the scalability of DNA barcoding. Moreover, existing DNA conjugation methods often employ non-site-specific approaches that target active functional groups on a limited number of amino acids (*e.g.*, lysine and cysteine). This can result in reduced signals and decreased antibody affinity and specificity[9,10]. Overcoming these obstacles is crucial for realizing the full potential of DNA barcoding in immunodetection applications.

Here, we present the *M*ultiplexed *a*nd *M*odular *B*arcoding of *A*ntibodies (MaMBA) strategy, a simple and cost-effective method of barcoding antibodies with single-stranded DNAs. To enhance modularity, MaMBA introduces nanobodies as adaptor proteins between the IgG antibodies and the barcode DNA oligos. Nanobodies are small (~15 kDa *v.s.* ~50 kDa for protein A, protein G, or the Fab fragments) and can be recombinantly expressed in large quantities. This modular design enables the rapid dissemination of the DNA barcoding method to a vast number of off-the-shelf antibodies. MaMBA employs an enzymatic reaction for site-specific conjugation of DNA oligos to nanobodies, rather than using chemical linkers, thereby minimizing potential adverse effects on nanobody affinity and specificity. We first combined MaMBA with the fluorescent signal amplification method *is*HCR (*i*mmuno*s*ignal *h*ybridization *c*hain *r*eaction) to establish a highly multiplexed and sensitive immunohistochemistry method for spatial protein profiling (*M*aMBA-assisted *is*HCR, *mis*HCR). To further increase the multiplex capacity of *mis*HCR, we designed a cleavable MaMBA variant, enabling the development of a multi-round version of *mis*HCR (*mis*HCR^{n}). Extending this strategy to the traditional enzyme-linked immunosorbent assay (ELISA), we developed a barcode-linked immunosorbent assay (BLISA) and demonstrated its utility in multiplexed and high-throughput detections of disease-associated

91 antigens, antibodies, and phosphoproteins.

92

Results

Design and validation of MaMBA

We used an enzymatic reaction to efficiently conjugate nanobodies with DNA oligos in a site-specific manner (**Fig. 1a**). The recombinant *Oldenlandia affinis* asparaginyl endopeptidase (*Oa*AEP1)[11,12] is employed to catalyze the ligation of an azide-bearing dipeptide substrate (Gly-Val, GV) to the nanobodies at the tripeptide recognition motif (Asn-Gly-Leu, NGL) fused at the C-termini. The resulting azide-functionalized nanobodies can subsequently be covalently tagged with DNA oligos of desired sequences and lengths via a single-step click reaction (**Fig. 1a**,**b**). We chose nanobodies that selectively and monovalently bind to the fragment crystallizable (Fc) region of the IgG[13], thereby minimizing the potential interference with antigen recognition by the IgG. This property enables modular barcoding of antibodies through the straightforward combination of off-the-shelf primary IgG antibodies with DNA oligo-conjugated nanobodies (Nb-DNA oligos) (**Fig. 1c**). For the initial proof-of-principle demonstrations, we tested two IgG secondary nanobodies: TP897 (for rabbit IgGs), and TP1107 (specific for mouse IgGs)[13]. After tagging each IgG antibody with a unique DNA barcode, multiple antibodies can then be pooled together for subsequent applications (**Fig. 1c**).

To assess the efficiency of the *Oa*AEP1-mediated reaction for adding azide functional group to the nanobody and the efficiency of the click reaction for nanobody-DNA oligo conjugation, we performed SDS-PAGE gel electrophoresis of the protein products from each step (**Supplementary Fig. 1**). We observed high efficiency for both conjugation steps (86.8% for the *Oa*AEP1-mediated reaction (**Supplementary Fig. 1a**,**b**) and 92.9% for nanobody-DNA oligo conjugation (**Supplementary Fig. 1c**,**d**). We further measured the labeling degree of DNA molecules on IgG by MaMBA. We barcoded an anti-GFP IgG antibody with 62-bp DNA oligos

using MaMBA alongside two classic conjugation methods (**Supplementary Fig. 2**). For both amine- and thiol-targeted conjugation, increasing the DNA:antibody ratio in the reactions enhanced conjugation efficiency but resulted in substantially higher labeling degree, which refers to the number of labels attached per antibody molecule (**Supplementary Fig. 2a-c**). In stark contrast, MaMBA consistently labeled the antibodies with the same degree (1-2 DNA molecules per IgG), irrespective of the reaction conditions (**Supplementary Fig. 2d**). We further examined the effects of DNA conjugation on the antibody's binding ability. We performed Western Blot to detect GFP in cell lysates using DNA-labeled IgG antibodies. Under identical DNA-to-antibody ratios (3:1 or 15:1) in the conjugation reactions, antibodies generated by MaMBA exhibited superior GFP detection compared to those generated by amine- or thiol-targeted methods (**Supplementary Fig. 2e**). The sensitivity of amine- or thiol-conjugated antibodies in detecting GFP deteriorated dramatically as the DNA-to-antibody ratio (3:1, 15:1, and 25:1) increased in the conjugation reactions (*i.e.*, antibodies have higher labeling degree; **Supplementary Fig. 2e**). These results demonstrate the high efficiency and accuracy of MaMBA for antibody DNA barcoding.

Multiplexed *in situ* biomolecule imaging by *mis*HCR

We evaluated the capability of MaMBA for multiplexed *in situ* biomolecule imaging using immunofluorescence techniques. In the original *is*HCR protocol that we developed for amplifying immunosignals[14], we conjugated HCR initiators to secondary antibodies via a streptavidin-biotin bridge. While effective, this approach necessitates four mandatory steps prior to HCR reactions (**Extended Data Fig. 1a**) and faces multiplexity limitations due to the use of streptavidin. To address these constraints, we used MaMBA to tag primary antibodies with HCR

initiator-conjugated nanobodies. The resulting HCR initiator-primary antibody complexes (Ab-HCR initiator) can be directly applied to tissue samples, followed by HCR amplification (**Extended Data Fig. 1a**). MaMBA allows for the large-scale preparation and long-term storage of these key reagents, including the nanobody-HCR initiator conjugation and the MaMBA-barcoded primary antibodies, thereby effectively simplifies the *is*HCR procedure to a single immunostaining step. We named this new protocol *M*aMBA-assisted *is*HCR (*mis*HCR). To examine *mis*HCR's performance in tissue samples, we immunostained mouse brain sections against two target antigens (*e.g.*, neuronal nuclei (NeuN) or tyrosine hydroxylase (Th)) using *mis*HCR or antibodies tagged with fluorophore-conjugated nanobodies (**Extended Data Fig. 1b**; see Methods). *mis*HCR drastically increased the fluorescence signals (**Extended Data Fig. 1b-d**) and preserved spatial resolution for diffraction-limited confocal imaging (**Extended Data Fig. 1e-g**).

We next asked whether *mis*HCR has a high multiplexity capacity (**Extended Data Fig. 2a**). By barcoding primary antibodies with orthogonal HCR initiators, *mis*HCR resolves the constraints imposed by antibody host species and enables simultaneous immunostaining of multiple targets in the same sample. Visualization of antigen-antibody-HCR initiator complexes is achieved through orthogonal HCR amplification reactions. To resolve the issue of spectral overlaps among fluorescent reporters, we established a protocol for the efficient removal of fluorescence signals from previous HCR amplifications through formamide-mediated dehybridization of HCR amplifiers (**Extended Data Fig. 2b**; see Methods). We validated this approach by conducting five consecutive cycles of HCR amplification/formamide treatment in immunostaining mouse brain sections against NeuN and Neurofilament H (NF-H) (**Extended Data Fig. 2c**). Statistical analysis revealed no significant differences in fluorescence intensity

between consecutive rounds (**Extended Data Fig. 2d**), with over 80% of fluorescence signals retained after four rounds of formamide treatment **(Extended Data Fig. 2d**). Thus, formamide did not significantly disrupt the antigen-Ab-HCR initiator complexes nor impaired the subsequent HCR amplification reactions, allowing for sequential rounds of HCR amplification and thus highly reproducible immunofluorescence detection.

As a demonstration of its potential, we applied *mis*HCR for multiplexed immunostaining on skin biopsies from healthy donors or patients with psoriasis (**Fig. 1d**). We used four rabbit IgG antibodies and two mouse IgG1 antibodies to detect markers of six cell types. *Mis*HCR successfully revealed distinct patterns of each cell type (**Fig. 1d**). Consistent with previous findings[15,16], the skin biopsies from psoriasis patients exhibited dilated blood vessels, accumulation of white blood cells, and abnormal proliferation of keratinocytes (**Fig. 1d** and **Extended Data Fig. 3**).

To further enhance the multiplexing capability of *mis*HCR, we developed a cleavable variant of MaMBA which incorporates an additional disulfide linker between the nanobody and the conjugated DNA oligo (**Fig. 2a**). Upon exposure to reducing agents such as tris(2-carboxyethyl)phosphine (TCEP), the disulfide linker undergoes reductive cleavage, releasing the conjugated DNA oligo from the nanobody. By integrating this cleavable MaMBA tagging with *mis*HCR, all HCR initiators (and their associated hybridized HCR amplifiers) can be removed from the samples post-imaging (**Extended Data Fig. 4**; see Methods). This approach enables the reuse of the same set of HCR initiators with additional antibodies in subsequent rounds of immunostaining. Through iterative cycles of multiplexed immunostaining, sequential HCR amplification, imaging, and HCR initiator removal, we achieve highly flexible and multiplexed *in situ* biomolecule detection (**Fig. 2b**). We named this new pipeline as *mis*HCR^{n}.

We validated *mis*HCR^{n} by immunostaining mouse brain sections against nine target antigens with well-defined and distinct distributions (**Extended Data Fig. 5a**). We used nine rabbit IgG antibodies and three orthogonal HCR initiators to perform three rounds of *mis*HCR (*mis*HCR^{3}). All targets were successfully visualized (**Extended Data Fig. 5a**). Protein markers for cell types showed distinct and non-overlapping distributions (**Extended Data Fig. 5b**). No cross-reaction among barcoded antibodies from the same or different rounds of *mis*HCR was observed. We then further demonstrated a twelve-antigen *in situ* imaging in the dorsal raphe nucleus (DRN) of mouse brain sections by two rounds of *mis*HCR (*mis*HCR^{2}) using twelve rabbit IgG antibodies with nine orthogonal HCR initiators (**Fig. 2c**). Additional control immunostaining experiments confirmed the specificity of *mis*HCR on all twelve targets (**Extended Data Fig. 6**; see Methods). We again observed precise distributions of target antigens. In particular, by analyzing the co-localization among DOPA decarboxylase (Ddc), tyrosine hydroxylase (Th), tryptophan hydroxylase 2 (Tph2), and 5-hydroxytryptamine (5-HT), we were able to identify three types of Ddc-expressing neurons in the DRN: likely dopamine neurons ($Ddc^{+}Th^{+}Tph2^{-}$), likely 5-HT neurons ($Ddc^{+}Th^{-}Tph2^{+}$), and the non-dopamine and non-5-HT neurons ($Ddc^{+}Th^{-}Tph2^{-}5\text{-}HT^{-}$)[17] (**Fig. 2d**). These results demonstrate that *mis*HCR utilizing MaMBA for antibody barcoding allows specific, flexible, and highly multiplexed *in situ* biomolecule imaging of animal and human clinical samples.

Barcode-linked immunosorbent assay (BLISA)

Building on the success of MaMBA-based immunofluorescent imaging, we next explored the potential of MaMBA for high-throughput, quantitative assays of diverse biomolecules. The enzyme-linked immunosorbent assay (ELISA) has long been a cornerstone technique in

diagnostics and research for quantitative biomolecule analysis. Standard ELISA assays predominantly rely on enzymatic reactions that utilize horseradish peroxidase (HRP) or alkaline phosphatase to convert chromogenic substrates for sensitive signal readout. However, the limited availability of orthogonal enzyme-substrate pairs typically necessitates separate ELISA reactions for detecting multiple antigens within a single sample. To enhance multiplexing capacity, we integrate the cleavable version of MaMBA into the classic ELISA. We label antibodies targeting different antigens with DNA oligos harboring orthogonal barcode sequences (DNA barcodes), so the labeled antibodies can be applied to the sample simultaneously. Following the removal of excessive antibodies that do not bind antigens, the DNA oligos are retrieved via the reductive cleavage for readout, which reduces potential interference from other DNAs (*e.g.*, genome DNA). The quantity of target molecules in the samples can then be inferred by quantifying the corresponding DNA barcodes. We named this multiplexed biomolecule detection protocol BLISA.

We first established the BLISA protocol by detecting antigens that are directly immobilized on microplate surfaces (**Fig. 3a**). We spiked recombinant GFP and mCherry proteins into cell lysates at varying concentrations. Each sample contained an equal amount of cell lysate, with the concentrations of GFP and mCherry adjusted to create a gradient (**Fig. 3b**). We simultaneously detected GFP, mCherry, and α-tubulin (an endogenous protein in the cell lysates) by a pool of three cleavable DNA-barcoded primary antibodies (Ab-SS-DNA barcodes), each specific to one antigen and tagged with a unique DNA oligo containing a distinct PCR handle sequence. The DNA barcodes were released by the reductant (*i.e.*, TCEP) and quantified via orthogonal qPCR (**Fig. 3a**,**b**). Three targets were successfully detected by qPCR in all sample groups (**Fig. 3c**). The ΔCt of qPCR reactions detecting GFP and mCherry in each group were

well fitted with the predetermined concentration gradients of GFP and mCherry (**Fig. 3d**, R^2 = 0.9945 and 0.9973, respectively).

We then examined the performance of BLISA over cell lysates containing endogenously expressed GFP or mCherry. We used two drug-inducible gene expression systems (*i.e.*, the tetracycline-regulated gene expression system and the cAMP response element-mediated gene expression system) to drive varying expression levels of GFP and mCherry in the cells (**Extended Data Fig. 7a**,**d**; see Methods). We applied BLISA to simultaneously detect GFP/mCherry and α-tubulin (as the loading control). In parallel, we also conducted Western blotting of GFP, mCherry, and α-tubulin on the same samples (**Extended Data Fig. 7b**,**e**; see Methods). The detection results obtained from BLISA demonstrated high correlation with those from Western blotting (**Extended Data Fig. 7c**,**f**). We obtained similar results when GFP and mCherry were co-expressed in the same cells (**Fig. 3e**-**g**).

To further evaluate its multiplexity, we applied BLISA to simultaneously detect the phosphorylation of multiple target proteins. We implemented BLISA in a magnetic bead-based sandwich immunoassay format, wherein target proteins were immobilized by capture antibodies covalently attached to the magnetic beads and subsequently detected using a pool of DNA-barcoded detection antibodies (**Fig. 4a**). We compared the sensitivity of magnetic bead-based BLISA with classic ELISA for detecting seven phosphorylated proteins (**Extended Data Fig. 8a**,**b**; see Methods). The resulting standard curves demonstrated that BLISA exhibited either superior or comparable sensitivity to ELISA for all seven targets (**Extended Data Fig. 8a**). To assess the specificity of the magnetic bead-based BLISA, we prepared mixtures of the seven purified phosphorylated proteins at varying concentration gradients (**Extended Data Fig. 8c**). The BLISA-detected concentrations of all phosphorylated proteins closely aligned with their

predetermined concentration gradients (R^2 = 0.9544, 0.9663, 0.9197, 0.9948, 0.9938, 0.9939, and 0.9198, respectively), with no significant cross-reactivity observed between different targets (**Extended Data Fig. 8c**).

Following the protocol validation, we applied the 7-plex magnetic bead-based BLISA to examine the effects of various treatments on the levels of seven phosphoproteins in U87 and U937 cells (non-treated, 10% FBS for 10 min, 100 nM anisomycin for 1 h, and 20 mM H_2O_2 for 10 min) (**Fig. 4b**). To facilitate a comparative analysis, cells were lysed and the resulting lysates were aliquoted for BLISA and ELISA (*n* = 3 replicates for BLISA; *n* = 2 replicates for each phosphoprotein and =14 in total for ELISA). Results of the 7-plex BLISA were well correlated with ELISA (**Fig. 4b**). Importantly, magnetic bead-based BLISA demonstrated superior multiplex capability by simultaneously detecting all phosphoproteins within individual samples. In contrast, ELISA necessitated separate aliquots for each phosphoprotein assay. This key distinction underscores BLISA's advantages in terms of efficiency, sample conservation, and cost-effectiveness.

A key feature of BLISA is its adaptability to a wide range of DNA-based technologies. We developed a high-throughput version of BLISA by incorporating next-generation sequencing (NGS) for simultaneous readout of DNA barcodes from multiple samples. We labeled individual antibody molecules with DNA oligos containing an antibody-specific 6-bp barcode sequence (Ab-bc) and a 15-bp unique molecular identifier (UMI) for quantification[18] (**Extended Data Fig. 9a**). Following retrieval from antigen-antibody complexes via TCEP cleavage, the DNA barcodes were further tagged with a well-specific barcode (well-bc) through PCR amplification (**Extended Data Fig. 9a**). Subsequently, DNA barcodes from separate BLISA reactions were pooled together to prepare an indexed library for sequencing. This approach enables

identification of each analyte in different samples through unique combinations of Ab-bcs and well-bcs, with quantification based on corresponding UMI counts. To validate the sequencing-based BLISA, we applied it to cell lysates spiked with varying concentrations of GFP and mCherry. The results demonstrated a high correlation between the sequencing-derived quantities of GFP and mCherry and their predetermined concentration gradients (R^2 = 0.9827 and 0.9843, respectively) (**Extended Data Fig. 9b**,**c**).

To demonstrate the potential of BLISA for high-throughput drug screening, we utilized an HTS-based 8-plex BLISA to the effects of 90 FDA-approved small-molecule compounds on U87 cells. The selected compounds were either kinases inhibitors exhibiting high blood-brain-barrier penetrance or drugs previously reported to inhibit GBM cell proliferation or migration (detailed compound information is listed in **Supplementary Table 1**). Cells were treated with 10 μM of each compound or DMSO (vehicle control) for 24 hours. As a positive control, cells were treated with 1mM pervanadate for 30 min. The magnetic bead-based BLISA was performed to simultaneously detect the phosphorylation of seven proteins and the level of GAPDH as a loading control. The screen was performed in duplicate. Among the 90 compounds, we identified PFK15 as a potent inducer for the phosphorylation of all seven target proteins (z-scores > 2; **Fig. 4c**). This finding was subsequently verified by individual ELISA specific to each target protein (**Fig. 4d**). These results show that BLISA can utilize the NGS technology to dramatically increase the throughput.

BLISA for high-throughput IgG detection in human serum.

We asked whether BLISA could detect biomolecules in clinical samples with high throughput. The increasing threat posed by zoonotic diseases, as exemplified by the severe acute

respiratory syndrome coronavirus 2 (SARS-CoV-2) pandemic, underscores the need for serologic surveillance methods to monitor population immunity[19,20]. We applied the sequencing-based BLISA to human serum samples to detect IgG antibodies recognizing the SARS-CoV-2 spike receptor binding domain (RBD)[21,22]. We first compared the sensitivity of BLISA and the standard ELISA method for human IgG detection (**Extended Data Fig. 10a**). BLISA significantly outperforms ELISA, demonstrating approximately 49-fold higher sensitivity and an approximately 0.15 logs wider dynamic range (**Extended Data Fig. 10b**).

We then applied an indirect sandwich immunoassay to detect the anti-RBD IgGs in human serum samples: the anti-RBD IgGs were captured by the immobilized RBD proteins and were detected by the DNA-barcoded anti-human IgG antibody (**Fig. 5a**). We first applied qPCR-based BLISA in serum samples from 24 donors who voluntarily disclosed their SARS-CoV-2 vaccination records. Of these, 23 had received at least one dose of an inactivated SARS-CoV-2 vaccine, while one donor had neither been vaccinated nor tested positive for SARS-CoV-2 (the negative control). We obtained anti-RBD IgG quantifications that were highly consistent with those acquired by ELISA (**Extended Data Fig. 10c**). The anti-RBD IgG level of the negative control sample was indeed lower than those from vaccinated donors (**Extended Data Fig. 10c**). Considerable variations in the anti-RBD IgG levels were observed among samples from vaccinated donors (**Extended Data Fig. 10c**), indicating differential vaccination status and/or immune responses. Subsequently, we conducted HTS-based BLISA on a cohort of 517 human serum samples (including the 24 serum samples), the majority of which (n = 493) were collected from healthy individuals undergoing routine physical examinations during the initial phase of the SARS-CoV-2 vaccination campaign in Beijing, China. Each serum sample was assayed in duplicates (1034 reactions in separated wells; twelve 96-well plates). As a technical control, 12

samples from vaccinated donors were randomly selected and distributed across 12 different BLISA plates. For each plate, we also included the negative control sample as well as a blank sample (without serum input). To mitigate sample-to-sample variations potentially introduced during sequencing library preparation, we spiked additional normalization DNA oligos into samples during the barcode retrieval step (**Fig. 5a**; **Extended Data Fig. 11a**,**b**; see Methods). The variation between duplicates was substantially reduced after normalization, with 98.4% of samples exhibiting a coefficient of variation (CV) below 0.2 (**Extended Data Fig. 12a**). No significant plate-to-plate variation in the detection results was observed (**Extended Data Fig. 12b**,**c**). The quantifications by HTS-based BLISA were highly consistent between technical duplication (**Fig. 5b**). The anti-RBD IgG levels of the 12 samples from vaccinated donors quantified by HTS-based BLISA were again highly consistent with ELISA measurements (**Fig. 5c-e**). Notably, the anti-RBD IgG levels of the majority of assayed samples (95.7%, measured using a threshold at three standard deviations above the mean of the negative samples) were higher than those of the negative samples (**Fig. 5f**). This result aligns with the high vaccination rate during the time period in Beijing, China when the samples were collected.

High-throughput 2-plex BLISA for human Hepatitis B virus (HBV) diagnosis

We performed 2-plex BLISA for the simultaneous detection of hepatitis B surface antigen (HBsAg) and hepatitis B e antigen (HBeAg) in serum samples. These two serological markers are crucial for the diagnosis and monitoring of hepatitis B virus (HBV) infection. The significant difference in the physiological concentrations of these antigens in blood (HBsAg being substantially more abundant than HBeAg[23]) presents a considerable challenge for concurrent detection. We again utilized a sandwich immunoassay format: both antigens (HBsAg

and HBeAg) were captured by their respective immobilized capture antibodies (Ab^{Cap}) and subsequently detected using DNA-barcoded detection antibodies (Ab^{Det}-SS-DNA barcode) (**Fig. 6a**). For the initial test, we obtained a cohort of 529 human serum samples (designated as cohort 1). These samples were analyzed in parallel (in duplicate; 1,058 reactions in separated wells on twelve 96-well plates) (**Supplementary Fig. 3a**). We employed differential concentrations of detection antibodies: anti-HBsAg at 0.33 nM and anti-HBeAg at 0.033 nM, as recommended by the manufacturer (detailed antibody information in **Supplementary Table 2**). This ten-fold difference in antibody concentration resulted in significant variations in read number distribution between HBsAg and HBeAg in the sequencing data (**Supplementary Fig. 3b**). Importantly, despite these differences, the simultaneous detection of these two antigens within the same BLISA assay remained unaffected. For both the HBsAg and HBeAg, the detections were highly consistent between the duplicate ($r = 0.9973$, $P < 0.0001$; $r = 0.9770$, $P < 0.0001$) (**Supplementary Fig. 3c**). The levels of both HBsAg and HBeAg detected by BLISA were significantly higher in the positive control samples than in the negative control samples (**Supplementary Fig. 3d**).

To validate our results, we performed ELISA on a subset of 115 samples and identified 28 $HBsAg^+$ samples and 7 $HBeAg^+$ samples (**Supplementary Fig. 3e**,**g**). We analyzed the sensitivity and specificity of BLISA on this ELISA-confirmed subset. The threshold for positive sample identification in the BLISA dataset was set at three standard deviations above the mean of the ELISA-confirmed negative samples (**Supplementary Fig. 3e**,**g**). For HBsAg, BLISA achieved a sensitivity of 100% (95% CI, 87.94% to 100.0%) and a specificity of 96.55% (95% CI, 90.35% to 99.06%) in discriminating ELISA-confirmed negative and positive samples (**Supplementary Fig. 3e**,**f**). For HBeAg, BLISA achieved a sensitivity of 100% (95% CI, 64.57%

to 100.0%) and a specificity of 96.30% (95% CI, 90.86% to 98.55%) in discriminating ELISA-confirmed negative and positive samples (**Supplementary Fig. 3g**,**h**).

We next collected a new cohort of serum samples from 600 donors (designated as cohort 2). To ensure enough positive samples for statistical analysis, this new cohort included 100 samples from donors that have been clinically diagnosed as HBV positive. To establish a reference standard for analyzing the specificity and sensitivity of BLISA, we performed ELISA on all samples and identified 119 $HBsAg^+$ samples and 90 $HBeAg^+$ samples (**Fig. 6b**,**d**). Subsequently, we performed HTS-based BLISA on this new cohort (in duplicate; 1,200 reactions in separated wells on fourteen 96-well plates). The detections of both the HBsAg and HBeAg were again highly consistent between the duplicate ($r = 0.9712$, $P < 0.0001$; $r = 0.9703$, $P < 0.0001$) (**Fig. 6f**). For HBsAg, BLISA achieved a sensitivity of 92.4% (95% CI, 86.25% to 95.97%) and a specificity of 99.1% (95% CI, 97.80% to 99.66%) in discriminating ELISA-confirmed negative and positive samples (**Fig. 6b**,**c**). For HBeAg, BLISA achieved a sensitivity of 93.3% (95% CI, 86.21% to 96.91%) and a specificity of 99.6% (95% CI, 98.57% to 99.93%) in discriminating ELISA-confirmed negative and positive samples (**Fig. 6d**,**e**).

We conducted additional analyses wherein the thresholds for positive sample identification in the BLISA datasets were established independently of ELISA data. Considering the low prevalence of HBV infection in the general Chinese population, recently estimated at 3% (95% CI: 2–4%)[24], we set the threshold for positive sample identification in the BLISA dataset at one standard deviation above the mean of the entire cohort (**Supplementary Fig. 4**). This approach was based on the assumption that the majority of samples in our two cohorts would be negative for HBsAg and HBeAg. We calculated the threshold for cohort 1 (529 samples) and applied it to the 115 ELISA-confirmed samples in cohort 1 (**Supplementary Fig. 4a**,**b**). For

HBsAg, BLISA achieved a sensitivity of 92.86% (95% CI, 77.35% to 98.73%) and a specificity of 100% (95% CI, 95.77% to 100%) in discriminating ELISA-confirmed negative and positive samples (**Supplementary Fig. 4a**). For HBeAg, BLISA achieved a sensitivity of 100% (95% CI, 64.57% to 100%) and a specificity of 94.44% (95% CI, 88.41% to 97.43%) in discriminating ELISA-confirmed negative and positive samples (**Supplementary Fig. 4b**). Similarly, we calculated the threshold for cohort 2 (based on 500 samples in cohort 2, excluded 100 positive control samples; **Supplementary Fig. 4c**,**d**). For HBsAg, BLISA achieved a sensitivity of 90.76% (95% CI, 84.20% to 94.76%) and a specificity of 99.78% (95% CI, 98.78% to 99.99%) in discriminating ELISA-confirmed negative and positive samples (**Supplementary Fig. 4c**). For HBeAg, BLISA achieved a sensitivity of 91.11% (95% CI, 83.43% to 95.43%) and a specificity of 99.80% (95% CI, 98.89% to 99.99%) in discriminating ELISA-confirmed negative and positive samples (**Supplementary Fig. 4d**). These results thus demonstrate that BLISA enables multiplexed and high-throughput detection of disease-related biomolecules in clinical samples with high specificity and sensitivity.

Discussion

DNA-barcoded antibodies have been increasingly utilized to unravel the molecular characteristics of the crowded biological environment[4,6,25–30]. However, despite the extensive repertoire of commercially available antibodies, a universally applicable strategy for site-specific antibody-DNA conjugation remains elusive. Previous approaches often require custom conjugation protocols for individual antibodies and specific applications, resulting in labor-intensive and costly processes[31]. Furthermore, traditional non-site-specific approaches, which rely on random conjugation to specific amino acid residues (*e.g.*, lysine or cysteine), often

compromise antibody affinity and specificity due to potential modification of residues within or adjacent to antigen-binding sites. To address these limitations, site-directed antibody-DNA conjugation approaches have been developed by utilizing the non-canonical amino acids[32] or affinity reagents (*e.g.*, nitrilotriacetic acid[33], FCIII peptide[34], protein G[35] or the Z domain of protein A[36]). Nonetheless, these techniques typically yield low product quantities and necessitate multiple components or genetic re-engineering of the antibody.

The MaMBA strategy, developed in this study, offers a highly efficient and site-specific DNA barcoding approach that is broadly applicable to IgG antibodies. Classic antibody conjugation methods necessitate stringent reaction conditions to achieve optimal yields, typically requiring a minimum of 50-100 μg IgG antibodies at 1 mg/mL per reaction. For commercially available antibodies, the buffer recipe and the stock concentration vary significantly across manufacturers and may not be compatible with the conjugation reactions. Consequently, buffer exchange and antibody concentration adjustments are often necessary prior to the reaction. Additionally, both antibodies and DNA oligos require activation for subsequent conjugation, with the activated intermediates being unstable and necessitating fresh preparation before each reaction. These requirements collectively increase operational complexity and costs (**Supplementary Fig. 5**). By utilizing anti-IgG Fc nanobodies[13] as adaptors, MaMBA achieves a remarkable degree of modularity. The DNA oligos are site-specifically conjugated to the C-terminal of the anti-IgG Fc nanobodies through a highly efficient enzymatic reaction. This approach minimizes potential impacts on nanobody functionality while enabling large-scale production of DNA-nanobody barcoding modules with diverse DNA sequences. The monovalent binding nature of the anti-Fc nanobodies also simplifies the barcoding procedure to a single mixing step, thus offering significantly advantageous applicability. MaMBA shall promote the

widespread adoption of DNA-barcoded antibody-based technologies across a multitude of biomedical and diagnostic applications.

To demonstrate the utility of MaMBA, we employed this method to develop novel techniques for multi-channel *in situ* protein imaging (*mis*HCR^n) and high-throughput biomolecule detections (BLISA). The MaMBA-based *mis*HCR^n method enables *in situ* imaging of biomolecules with enhanced multiplexity and sensitivity compared to traditional immunohistochemistry, which is typically limited in the number of detectable biomolecules due to spectral and host species constraints. We initially developed the *is*HCR method to extend the multiplexing capability of immunohistochemistry through the use of HCR initiators with distinct DNA sequences[14]. However, the potential of *is*HCR remains constrained by the limited availability of orthogonal HCR initiator/amplifier pairs (*i.e.*, five pairs from the original HCR study and eight additional newly reported pairs[37]). MaMBA addresses these limitations by directly attaching HCR initiators to primary antibodies via a cleavable chemical linker, thereby simplifying the misHCR^n staining procedure and eliminating host species overlaps. Moreover, MaMBA enables the removal of HCR initiators after image acquisition using a mild reducing agent (*e.g.*, TCEP)[38], allowing for iterative uses of HCR initiator/amplifier pairs. We achieved 12-plex *mis*HCR^n immunodetection on mouse brain sections using 12 rabbit IgGs and a standard confocal imaging setup. The multiplexity and the imaging throughput of *mis*HCR^n can be further enhanced by incorporating advanced chemical probes and imaging techniques, such as Raman dyes[39,40] and spectral unmixing[41]. As a versatile antibody barcoding technique, the utility of MaMBA in immunohistochemistry extends beyond our demonstrations with *mis*HCR^n here. MaMBA could be readily employed in various existing DNA-based multiplexed

immunofluorescence methods, including DNA-Exchange (DEI)[42,43], CODEX[29,44], and immuno-SABER[28].

Leveraging the flexibility of the ELISA design, we utilized MaMBA to develop BLISA for multiplexed and quantitative biomolecule detections. Traditional ELISA typically relies on arrayed enzymatic reactions to report the quantities of target molecules in different samples. In contrast, MaMBA-based BLISA replaces the enzyme reporters with retrievable single-stranded DNA barcodes, enabling quantifications via qPCR or NGS technologies in a highly multiplexed and high-throughput way. Moreover, BLISA is compatible with various sample types (*e.g.*, serum and cell lysate) and assay formats (*e.g.*, plate- or beads-based assay). We successfully used BLISA to simultaneously measure the levels of anti-SARS-CoV-2-RBD antibody or HBV antigens in over 1,000 human serum samples. Moreover, we demonstrated an HTS-based 8-plex BLISA for a small-scale drug screen. Representing a high-throughput platform with dramatically enhanced multiplex capacity, BLISA effectively lowers the costs, sample-volume requirement, and turnaround time. Lab automation for sample handling and sequencing library preparation could further facilitate the adoption of BLISA in large-scale applications in both clinical diagnostics and translation research (*e.g.*, pandemic surveillance and biomarker discoveries). Additionally, other existing methods, including immuno-PCR[45,46], ID-seq[6,47], the proximity extension assay (PEA)[48,49] and single-cell sequencing-based protein profiling[25,26,50,51], would also benefit from our MaMBA approach.

References

1. Maynard, J. & Georgiou, G. Antibody Engineering. *Annu. Rev. Biomed. Eng.* **2**, 339–376 (2000).
2. Scott, A. M., Wolchok, J. D. & Old, L. J. Antibody therapy of cancer. *Nat. Rev. Cancer* **12**, 278–287 (2012).
3. Stack, E. C., Wang, C., Roman, K. A. & Hoyt, C. C. Multiplexed immunohistochemistry, imaging, and quantitation: A review, with an assessment of Tyramide signal amplification, multispectral imaging and multiplex analysis. *Methods* **70**, 46–58 (2014).
4. Lewis, S. M. *et al.* Spatial omics and multiplexed imaging to explore cancer biology. *Nat. Methods* **18**, 997–1012 (2021).
5. Rajagopalan, A. *et al.* SeqStain is an efficient method for multiplexed, spatialomic profiling of human and murine tissues. *Cell Rep. Methods* **1**, 100006 (2021).
6. van Buggenum, J. A. G. *et al.* Immuno-detection by sequencing enables large-scale high-dimensional phenotyping in cells. *Nat. Commun.* **9**, 2384 (2018).
7. Liszczak, G. & Muir, T. W. Nucleic Acid-Barcoding Technologies: Converting DNA Sequencing into a Broad-Spectrum Molecular Counter. *Angew. Chem. Int. Ed.* **58**, 4144–4162 (2019).
8. Zhong, W. *et al.* Next generation plasma proteome profiling to monitor health and disease. *Nat. Commun.* **12**, 2493 (2021).
9. Dovgan, I., Koniev, O., Kolodych, S. & Wagner, A. Antibody–Oligonucleotide Conjugates as Therapeutic, Imaging, and Detection Agents. *Bioconjug. Chem.* **30**, 2483–2501 (2019).
10. Dugal-Tessier, J., Thirumalairajan, S. & Jain, N. Antibody-Oligonucleotide Conjugates: A Twist to Antibody-Drug Conjugates. *J. Clin. Med.* **10**, 838 (2021).
11. Yang, R. *et al.* Engineering a Catalytically Efficient Recombinant Protein Ligase. *J. Am. Chem. Soc.* **139**, 5351–5358 (2017).
12. Rehm, F. B. H. *et al.* Site-Specific Sequential Protein Labeling Catalyzed by a Single Recombinant Ligase. *J. Am. Chem. Soc.* **141**, 17388–17393 (2019).
13. Pleiner, T., Bates, M. & Görlich, D. A toolbox of anti–mouse and anti–rabbit IgG secondary nanobodies. *J Cell Biol* **217**, 1143–1154 (2018).

14. Lin, R. *et al.* A hybridization-chain-reaction-based method for amplifying immunosignals. *Nat. Methods* (2018) doi:10.1038/nmeth.4611.

15. Lowes, M. A., Bowcock, A. M. & Krueger, J. G. Pathogenesis and therapy of psoriasis. *Nature* **445**, 866–873 (2007).

16. Bowcock, A. M. & Krueger, J. G. Getting under the skin: the immunogenetics of psoriasis. *Nat. Rev. Immunol.* **5**, 699–711 (2005).

17. Ikemoto, K. Importance of D-neuron research in neuropsychiatry. *Integr. Mol. Med.* **4**, (2017).

18. Islam, S. *et al.* Quantitative single-cell RNA-seq with unique molecular identifiers. *Nat. Methods* **11**, 163–166 (2014).

19. Wajnberg, A. *et al.* Robust neutralizing antibodies to SARS-CoV-2 infection persist for months. *Science* **370**, 1227–1230 (2020).

20. Khoury, D. S. *et al.* Neutralizing antibody levels are highly predictive of immune protection from symptomatic SARS-CoV-2 infection. *Nat. Med.* **27**, 1205–1211 (2021).

21. Hoffmann, M. *et al.* SARS-CoV-2 Cell Entry Depends on ACE2 and TMPRSS2 and Is Blocked by a Clinically Proven Protease Inhibitor. *Cell* **181**, 271-280.e8 (2020).

22. Lan, J. *et al.* Structure of the SARS-CoV-2 spike receptor-binding domain bound to the ACE2 receptor. *Nature* **581**, 215–220 (2020).

23. Kessler, D. A. & Jimenez, A. Chapter 13 - Hepatitis B Virus Screening. in *Transfusion Medicine and Hemostasis (Third Edition)* (eds. Shaz, B. H., Hillyer, C. D. & Reyes Gil, M.) 73–76 (Elsevier, 2019). doi:10.1016/B978-0-12-813726-0.00013-1.

24. Bai, S., Dang, W., Hong, W., Liao, W. & Smith, R. D. The prevalence of hepatitis B in Chinese general population from 2018 to 2022: a systematic review and meta-analysis. *BMC Infect. Dis.* **24**, 211 (2024).

25. Stoeckius, M. *et al.* Simultaneous epitope and transcriptome measurement in single cells. *Nat. Methods* **14**, 865–868 (2017).

26. Hwang, B. *et al.* SCITO-seq: single-cell combinatorial indexed cytometry sequencing. *Nat. Methods* **18**, 903–911 (2021).

27. Vistain, L. *et al.* Quantification of extracellular proteins, protein complexes and mRNAs in single cells by

534 proximity sequencing. *Nat. Methods* **19**, 1578–1589 (2022).

535 28. Saka, S. K. *et al.* Immuno-SABER enables highly multiplexed and amplified protein imaging in tissues.
536 *Nat. Biotechnol.* 1–11 (2019) doi:10.1038/s41587-019-0207-y.

537 29. Goltsev, Y. *et al.* Deep Profiling of Mouse Splenic Architecture with CODEX Multiplexed Imaging. *Cell*
538 **174**, 968-981.e15 (2018).

539 30. M, L., A, E., B, T., E, A. & S, F. Homogeneous antibody-based proximity extension assays provide
540 sensitive and specific detection of low-abundant proteins in human blood. *Nucleic Acids Res.* **39**, (2011).

541 31. Hickey, J. W. *et al.* Spatial mapping of protein composition and tissue organization: a primer for
542 multiplexed antibody-based imaging. *Nat. Methods* **19**, 284–295 (2022).

543 32. Kazane, S. A. *et al.* Site-specific DNA-antibody conjugates for specific and sensitive immuno-PCR. *Proc.*
544 *Natl. Acad. Sci.* **109**, 3731–3736 (2012).

545 33. Rosen, C. B. *et al.* Template-directed covalent conjugation of DNA to native antibodies, transferrin and
546 other metal-binding proteins. *Nat. Chem.* **6**, 804–809 (2014).

547 34. Nielsen, T. B. *et al.* Peptide-Directed DNA-Templated Protein Labelling for The Assembly of a Pseudo-
548 IgM. *Angew. Chem. Int. Ed.* **58**, 9068–9072 (2019).

549 35. Cremers, G. A. O., Rosier, B. J. H. M., Riera Brillas, R., Albertazzi, L. & de Greef, T. F. A. Efficient
550 Small-Scale Conjugation of DNA to Primary Antibodies for Multiplexed Cellular Targeting. *Bioconjug.*
551 *Chem.* **30**, 2384–2392 (2019).

552 36. Stiller, C. *et al.* Fast and Efficient Fc-Specific Photoaffinity Labeling To Produce Antibody–DNA
553 Conjugates. *Bioconjug. Chem.* **30**, 2790–2798 (2019).

554 37. Wang, Y. *et al.* Multiplexed in situ protein imaging using DNA-barcoded antibodies with extended
555 hybridization chain reactions. *Nucleic Acids Res.* **52**, e71 (2024).

556 38. Pham, T., Nazaroff, C. D., Labaer, J. & Guo, J. Ultrasensitive and Multiplexed Protein Imaging with
557 Cleavable Fluorescent Tyramide and Antibody Stripping. *Int. J. Mol. Sci.* **22**, 8644 (2021).

558 39. Wei, L. *et al.* Super-multiplex vibrational imaging. *Nature* **544**, 465–470 (2017).

559 40. Shi, L. *et al.* Highly-multiplexed volumetric mapping with Raman dye imaging and tissue clearing. *Nat.*
560 *Biotechnol.* 1–10 (2021) doi:10.1038/s41587-021-01041-z.

41. Seo, J. *et al.* PICASSO allows ultra-multiplexed fluorescence imaging of spatially overlapping proteins without reference spectra measurements. *Nat. Commun.* **13**, 2475 (2022).

42. Wang, Y. *et al.* Rapid Sequential in Situ Multiplexing with DNA Exchange Imaging in Neuronal Cells and Tissues. *Nano Lett.* **17**, 6131–6139 (2017).

43. Jungmann, R. *et al.* Multiplexed 3D cellular super-resolution imaging with DNA-PAINT and Exchange-PAINT. *Nat. Methods* **11**, 313–318 (2014).

44. Black, S. *et al.* CODEX multiplexed tissue imaging with DNA-conjugated antibodies. *Nat. Protoc.* **16**, 3802–3835 (2021).

45. Sano, T., Smith, C. L. & Cantor, C. R. Immuno-PCR: Very Sensitive Antigen Detection by Means of Specific Antibody-DNA Conjugates. *Science* **258**, 120–122 (1992).

46. Niemeyer, C. M., Adler, M. & Wacker, R. Detecting antigens by quantitative immuno-PCR. *Nat. Protoc.* **2**, 1918–1930 (2007).

47. Buggenum, J. A. G. L. van *et al.* A covalent and cleavable antibody-DNA conjugation strategy for sensitive protein detection via immuno-PCR. *Sci. Rep.* **6**, 1–12 (2016).

48. Fredriksson, S. *et al.* Protein detection using proximity-dependent DNA ligation assays. *Nat. Biotechnol.* **20**, 473–477 (2002).

49. Wik, L. *et al.* Proximity Extension Assay in Combination with Next-Generation Sequencing for High-throughput Proteome-wide Analysis. *Mol. Cell. Proteomics MCP* **20**, 100168 (2021).

50. Chung, H. *et al.* Joint single-cell measurements of nuclear proteins and RNA in vivo. *Nat. Methods* **18**, 1204–1212 (2021).

51. Mimitou, E. P. *et al.* Multiplexed detection of proteins, transcriptomes, clonotypes and CRISPR perturbations in single cells. *Nat. Methods* **16**, 409–412 (2019).

52. Choi, H. M. T., Beck, V. A. & Pierce, N. A. Next-Generation in Situ Hybridization Chain Reaction: Higher Gain, Lower Cost, Greater Durability. *ACS Nano* **8**, 4284–4294 (2014).

53. Wang, Y. *et al.* Multiplexed in situ protein imaging using DNA-barcoded antibodies with extended hybridization chain reactions. *bioRxiv* 274456 (2020) doi:10.1101/274456.

54. Harris, K. S. *et al.* Efficient backbone cyclization of linear peptides by a recombinant asparaginyl

endopeptidase. *Nat. Commun.* **6**, 1–10 (2015).

55. Fabricius, V., Lefèbre, J., Geertsema, H., Marino, S. F. & Ewers, H. Rapid and efficient C-terminal labeling of nanobodies for DNA-PAINT. *J. Phys. Appl. Phys.* **51**, 474005 (2018).
56. Schindelin, J. *et al.* Fiji: an open-source platform for biological-image analysis. *Nat. Methods* **9**, 676–682 (2012).
57. Preibisch, S., Saalfeld, S., Schindelin, J. & Tomancak, P. Software for bead-based registration of selective plane illumination microscopy data. *Nat. Methods* **7**, 418–419 (2010).
58. Mölder, F. *et al.* Sustainable data analysis with Snakemake. *F1000Research* **10**, 33 (2021).
59. Smith, T., Heger, A. & Sudbery, I. UMI-tools: modeling sequencing errors in Unique Molecular Identifiers to improve quantification accuracy. *Genome Res.* **27**, 491–499 (2017).
60. Cock, P. J. A. *et al.* Biopython: freely available Python tools for computational molecular biology and bioinformatics. *Bioinforma. Oxf. Engl.* **25**, 1422–1423 (2009).
61. Wickham, H. *et al.* Welcome to the Tidyverse. *J. Open Source Softw.* **4**, 1686 (2019).

Materials and Methods

Reagents and reagent preparation

Detailed sequences and modifications of DNA oligos are listed in **Supplementary Table 3**. Detailed sequences of the vectors used in this study are listed in **Supplementary Table 4**. DNA oligos were synthesized by Thermo Fisher Scientific, Genewiz, and Sangon Biotech. The sequences of HCR (initiators and amplifiers) are adopted from previous reports[52,53]. All oligos were dissolved in nuclease-free water (Thermo Fisher Scientific, AM9932) and stored at -20℃. Polypeptides (Gly-Val-Gly-Lys(N_3)-Arg-Gly, GVG-K(N_3)-RG) with azide modification on lysine residues were synthesized by Scilight-Peptide (Beijing, China). Sodium tetraborate decahydrate (NaB; S9640), Triton X-100 (T8787), dextran sulfate (D8906), TCEP (646547), Tween-20 (P9416), protease inhibitor cocktail (PIC; P8340), and TMB (T0440) were purchased from Sigma-Aldrich. 20× sodium chloride citrate (SSC) buffer (AM9763), sheared Salmon sperm DNA (sssDNA; AM9680), cell extraction buffer (FNN0011), and protein-free blocking buffer (PFBB; 37572) were purchased from Thermo Fisher Scientific. Phosphatase inhibitor cocktail (PPIC, 5870S) was purchased from Cell Signaling Technology. Dulbecco's Modified Eagle Medium (DMEM), Minimum Essential Medium (MEM), RPMI 1640 Medium, fetal bovine serum (FBS), and penicillin-Streptomycin were purchased from Gibco.

Protein expression and purification

Recombinant expression of *Oa*AEP1 (C247A) was performed as previously described[11,12,54]. Briefly, pET28a-His_6-Ubiquitin-*Oa*AEP1 (C247A) was transformed into *E.coli* SHuffle and the protein expression was induced overnight with 1 mM IPTG at 18℃. Cells were harvested by centrifugation, resuspended in lysis buffer (50 mM NaH_2PO_4, pH 8.0, 300 mM

NaCl, 10 mM imidazole), and lysed by sonication. Cell debris was cleared via 1 h centrifugation at 39,000 g at 4 °C. The supernatant was bound to Ni-NTA resins, washed with AEP wash buffer (50 mM NaH_2PO_4, pH 8.0, 0.3 M NaCl, 20 mM imidazole), and eluted with elution buffer (50 mM NaH_2PO_4, pH 8.0, 0.3 M NaCl, 250 mM imidazole). To self-activate *Oa*AEP1, the eluted fraction was diluted in PBS buffer and incubated overnight at room temperature (RT), with 1 mM EDTA and 0.5 mM TCEP added to the solution and the pH adjusted to 4.0 using glacial acetic acid. After being filtered by 0.22 μm membrane and 1:8 diluted in 50 mM Acetate at pH 4.0, the mature protein was purified further by cation exchange (HiTrap SP column) and eluted with a salt gradient [0-100% of storage buffer (50 mM sodium acetate, pH 4.0, 10% Glycerol, 1 M NaCl); 10 column volumes]. Fractions containing mature AEP were pooled and concentrated using a 10 K MWCO concentrator (Sartorius). The final product was analyzed by SDS-PAGE, quantified via A_{280} reading (NanoPhotometer® N60, IMPLEN) according to the protein molecular weight and extinctions coefficient, and then stored in aliquots at -80°C until use.

Nanobodies against the Fc domain of IgG (TP897 against rabbit IgG and TP1107 against mouse IgG1) were expressed and purified according to previously published methods[13,55]. Briefly, pET21a-TP897-NGL-His_6 and pET21a-TP1107-NGL-His_6 were transformed into *E.coli* SHuffle. Nanobody expression was induced for 16–18 h with 1 mM IPTG at 28°C. After being harvested by centrifugation, cells were resuspended in Nb lysis buffer (50 mM HEPES, pH 7.5, 300 mM NaCl, 5 mM Imidazole, 10% Glycerol) and lysed by sonication. Cell debris was removed by centrifugation, and the supernatant was applied to Co-NTA resins. The resins were washed with Nb wash buffer (20 mM HEPES, pH 7.5, 300 mM NaCl, 20 mM Imidazole, 10% Glycerol) and the His-tagged nanobodies were eluted with Nb elution buffer (20 mM HEPES, pH 7.5, 300 mM NaCl, 500 mM Imidazole, 10% Glycerol). The nanobodies were further

purified and buffer exchanged by size exclusion column (SEC) in Nb exchange buffer (20 mM HEPES, pH 7.5, 300 mM NaCl, 10% Glycerol). Fractions containing nanobodies were pooled and concentrated using Amicon 3 K MWCO concentrator (Millipore). Protein concentrations were determined by A_{280} reading as described above. Nanobodies were stored in aliquots at -80℃ until use.

pET28a-GFP and pET28a-mCherry were transformed into *E.coli* BL21(DE3). Protein expression was induced for 16–18 h with 0.5 mM IPTG at 16℃. GFP and mCherry were purified using Co-NTA resins as described above and were further purified by SEC in PBS. Proteins were concentrated using Amicon 10 K MWCO concentrator and quantified by A_{280} reading.

C-terminal labeling of nanobodies by *Oa*AEP1 reaction

Purified NGL-tagged nanobodies (Nb-NGL-His_6) were labeled C-terminally using GVG-K(N_3)-RG polypeptides by OaAEP1 reaction as previously described[12]. This was carried out by reacting 50 μM nanobody, 1 mM GVG-K(N_3)-RG, and 750 nM OaAEP1 (C247A) in reaction buffer (100 mM sodium phosphate buffer, pH 6.5, supplemented with 2 mM DTT) overnight by gentle shaking at RT. The reaction mixture was then 1:1 diluted in Nb lysis buffer and bound to Ni-NTA resins to remove GL-His_6 and unreacted His-tagged nanobodies. Resins were washed with Nb lysis buffer until A_{280} reached baseline. Flowthrough and wash fractions containing azide-labeled nanobodies were pooled, and the excess GVG-K(N_3)-RG polypeptides were removed using a 3,000 MWCO concentrator. The azide-labeled nanobodies (Nb-N_3) were quantified by A_{280} reading, analyzed by SDS-PAGE, and then stored at -20℃.

Nanobody-fluorophore conjugation

Azide-labeled nanobodies (40 μM) were mixed with 10-fold molar excess of DBCO-Cy3 (777366, Sigma-Aldrich) or DBCO-Cy5 (777374, Sigma-Aldrich) and incubated at RT with shaking for 4 hr. Excess fluorophores were removed by Zeba spin desalting column (7k MWCO) twice. Protein concentration and the degree of labeling (DOL) were measured by NanoPhotometer® N60 with dye correction.

Nanobody-DNA oligonucleotide conjugation

For Nb-SS-HCR initiator and Nb-SS-DNA barcode, we used DBCO-PEG_3-SS-NHS (10 mM in anhydrous DMSO; CP-2089, Conju-Probe, LLC) as the linker. HCR initiators and DNA barcodes modified with a 5' NH_2-C6 moiety were reacted with DBCO-PEG_3-SS-NHS (20-fold molar excess) in 0.091 M NaB (pH 8.5) at RT for 2 h by gentle shaking. To remove excess linker, oligonucleotides were precipitated by mixing with a one-tenth volume of 3 M sodium acetate (pH 5.2) and two volumes of cold absolute ethanol for 1 h at -20℃. After a 30-min spin at 20,000g at 4℃, the supernatant was removed, and the pellet was carefully rinsed twice with cold 70% ethanol. The pellet was then air-dried and re-dissolved in TE buffer.

The DBCO-PEG_3-SS-conjugated oligos or HCR initiators with a 5' DBCO moiety (2-fold molar excess) were mixed with 25 μM azide-labeled nanobodies and incubated at 4℃ with shaking for 16 h. The DNA oligo-conjugated nanobodies were analyzed by SDS-PAGE and then stored at -20℃.

DNA barcoding to IgG antibodies by MaMBA strategy

Antibodies were premixed with 3-fold molar excess of DNA oligo-conjugated nanobodies in 50 μL premixing buffer (0.1% BSA, 0.05% Triton X-100 in PBS) at RT with shaking for 1–3 h. The mixtures were then added to Amicon Ultra-0.5 100 K centrifugal filters and washed ten times with 400 μL PBS containing 0.05% Tween-20 and 5 mM EDTA. Alternatively, the mixtures were incubated with normal IgG-conjugated beads (Thermo Fisher, 10500C or 31903) for 10 min at RT and the flowthrough was collected. Purified DNA-barcoded antibodies were stored at 4℃ with 0.03% NaN_3 or at -20℃ with 50% glycerol and used within one week.

Mice

Animal care and use followed the approval of the Animal Care and Use Committee of the National Institute of Biological Sciences, Beijing (Approval ID: NIBSLuoM15C), in accordance with the Regulations for the Administration of Affairs Concerning Experimental Animals of China. C57BL/6N mice were purchased from Beijing Vital River Laboratory Animal Technology Co., Ltd (China), and adult (8–12 weeks old) mice of either sex were used. Mice were maintained with a 12-h light/dark photoperiod (light on at 8 AM) and were provided food and water *ad libitum*.

Tissue sample preparation for immunohistochemistry

Mice were anesthetized with an overdose of pentobarbital and perfused intracardially with PBS, followed by 4% paraformaldehyde (PFA; 4% (w/v) in PBS). Brains were dissected out and postfixed in 4% PFA for 4 h at RT. Samples were cryoprotected in 30% sucrose until they sank. Coronal sections (35 μm) were prepared on a Cryostat microtome (Leica CM1950).

Human skin samples were obtained surgically, from 28-year-old female arm skin with psoriasis and 23-year-old male healthy arm skin. Samples were embedded in O.C.T compound, frozen at -80℃, and sectioned into 30-μm-thick specimens. Skin sections were fixed in 4% PFA for 15 min and washed three times with PBS.

Immunostaining by *mis*HCR/*mis*HCR^{n}

Detailed information about antibodies and Nb-HCR initiators (or Nb-SS-HCR initiators) used in this study are listed in **Supplementary Table 2**. Samples were permeabilized with 0.3% Triton X-100 in PBS (PBST) and blocked with blocking buffer (2% BSA, 5 mM EDTA, 0.3% Triton X-100 in PBS) for 1 h at RT. MaMBA-generated Ab-HCR initiators (or Ab-SS-HCR initiators) were pooled and diluted into incubation buffer (1% BSA, 0.1% Triton X-100, 5 mM EDTA, 0.5 mg/mL sssDNA, 1% dextran sulfate, 150 mM NaCl, 0.05% NaN_3 in PBS) supplemented with excess corresponding Nb-NGL-His_6. Tissue sections were incubated with the Ab-HCR initiators (or Ab-SS-HCR initiators) pool at 4℃ for 12–16 h and then washed three times with washing buffer (2% BSA, 0.1% Triton X-100 in PBS) for 10 min. After being washed twice with PBS for 5 min, samples were postfixed using 5 mM $BS(PEG)_5$ (A35396, Thermo Fisher Scientific) in PBS for 1 h at RT, followed by quenching in Tris-buffered saline (TBS) for 10 min. For control immunostaining experiments, tissue sections were incubated with antibodies diluted in blocking buffer at 4℃ for 12–16 h and then washed three times in PBST, followed by (1) incubation with Nb-fluorophore or Nb-HCR initiator in incubation buffer for 2 h at RT; or (2) incubation with a mixture containing equal amounts of Cy3-conjugated anti-rabbit IgG antibody (111-165-008, Jackson ImmunoResearch) and Nb-HCR initiator (B4 I1) in incubation buffer for 2 h at RT. Samples were then washed three times with PBST.

Before performing the next round of *mis*HCR, tissue sections with anchored Ab-SS-HCR initiators were incubated with 50 mM TCEP in PBS (to remove HCR initiators via reductive cleavage) for 15 min at RT, followed by three washes with PBST. Samples were incubated in blocking buffer for 1 h at RT, and a new round of staining was performed as above.

For the experiment for spatial resolution measurement, HeLa cells were fixed in 4% PFA for 10 min, washed three times with PBST, and blocked with a blocking buffer for 30 min at RT. For the standard method (2nd Ab), cells were stained by antibodies against α-tubulin (1:4,000 diluted; T5168, Sigma-Aldrich) and Alexa Fluor (AF) 647-conjugated secondary antibodies (1:1,000 diluted; 715-605-151, Jackson ImmunoResearch). For *mis*HCR, cells were stained by Ab-HCR initiator (B4 I1), followed by HCR using AF647-conjugated amplifiers.

HCR amplification

The basic HCR amplification process was common to all the experiments. Samples were blocked in amplification buffer (5× SSC buffer, 0.1% (v/v) Tween-20, 10% dextran sulfate) at RT for 1 h. Each pair of fluorophore-conjugated HCR amplifiers was snap-cooled separately in 5× SSC buffer by being heated at 95°C for 90 s using a PCR machine, immediately cooled on ice for 5 min, and then kept in the dark at RT for over 30 min. The amplifiers were mixed in amplification buffer to a final concentration of 12.5 nM for each amplifier. Samples were incubated with HCR amplifiers overnight at RT and washed three times with 5× SSCT (5× SSC buffer, 0.1% Tween-20) before imaging. The incubation time for HCR reaction can be tuned by adjusting the concentration of HCR amplifiers.

To perform multi-round imaging, samples were washed twice with 50% formamide in 0.1× PBS at 37°C for 5 min to remove the hybridized amplifiers and then washed three times

with PBST. After imaging, HCR initiators and hybridized HCR amplifiers were removed by TCEP treatment as described above. Sections were blocked again in the amplification buffer for 1 h at RT to start the next round of HCR amplification.

Fluorescence imaging

For image acquisition, samples were mounted on microscope slides in 50% glycerol containing 1 μg/mL DAPI (D9542, Sigma-Aldrich). Confocal microscopy was mainly performed on a Zeiss LSM880 using a 20×/NA-0.8 or 100×/NA-1.45 objective, or on a Leica SP8 using a 20×/NA-0.75 or 10×/NA-0.40 objective. AF488 was visualized using a 488-nm laser; Cy3, AF546, and AF594 were visualized using a 552-nm laser; and Cy5 and AF647 were visualized using a 638-nm laser. The images were 1024×1024 or 512×512 pixels and acquired with a frame averaging of two. Images were processed using Zeiss ZEN, Leica LAS X, and FIJI[56], and colored for display using FIJI and Photoshop. For multi-round images, a basic alignment and registration were done by descriptor-based registration plugin[57] based on the DAPI channel of each image using FIJI.

For 6-color multiplexing of human skin samples by *mis*HCR, the entire experiment was performed with three image rounds (round 1, PDGFRα, KRT14, and DCT; round 2, CD31; round 3, αSMA and CD45). For 9-color multiplexing of mouse brain slices by *mis*HCR^{n}, three stain rounds with one image round of each were performed (1st *mis*HCR round, MAP2, DDC, and nNOS; 2nd *mis*HCR round, NeuN, Iba1, and GFAP; 3rd *mis*HCR round, Th, NF-H and Tph2). For 12-color multiplexing of mouse brain slices by *mis*HCR^{n}, two rounds of *mis*HCR were performed with four image rounds (round 1, nNOS and GFAP; round 2, NeuN, Th and NF-H;

round 3, Tph2 and Orexin A; round 4, GABA) and three image rounds (round 1, Tmem119 and DDC; round 2, 5-HT; round 3, Iba1) respectively.

Cell culture and transfection

HEK293T cells (ATCC CRL-3216) and HeLa cells (ATCC CCL-2) were cultured in DMEM supplemented with 10% (v/v) FBS, 100 units/mL penicillin, and 100 units/mL streptomycin at 37°C with 5% CO_2. U87 cells (ATCC HTB-14) were cultured in MEM with 10% FBS, 100 units/mL penicillin, and 100 units/mL streptomycin. U937 cells (ATCC CRL-1593.2) were cultured in RPMI 1640 Medium with 10% FBS, 100 units/mL penicillin, and 100 units/mL streptomycin.

Cells were seeded in a 24-well plate and grown to 70–90% viable. For immunostaining, cells were cultured on coverslips pretreated with poly-L-lysine solution (P8920, Sigma-Aldrich). Cell medium was replaced by fresh complete medium 2 h before transfection. For each well, 0.5 μg plasmid and 0.5 μL DNA transfection reagent (Neofect) were mixed in 50 μL serum-free medium and incubated for 15–20 min at RT. The mixture was added to the cells with further incubation for 18–24 h at 37°C with 5% CO_2 before assaying for transgene expression. For cells transfected with P_{Tight}-EGFP-*PGK*-rtTA, Tet system-approved FBS (Biological Industries) was used.

For magnetic bead-based BLISA, cells were seeded in 6-well ($2–3 \times 10^5$ /well) and grown for 24 h in complete medium. Cells were subjected to an overnight starvation protocol or cultured in the presence of 0.2% FBS condition for a designated duration prior to drug treatments.

Drug treatment and cell lysis

HEK293T cells transfected with P_{Tight}-EGFP-*PGK*-rtTA were treated with ATc (541642, J&K) at varying concentrations (0–10 μM). HEK293T cells transfected with *3×CRE*-mCherry-PEST were treated with FSK (F3917, Sigma-Aldrich) at varying concentrations (0–100 μM) in the presence of 0.3 mM 3-Isobutyl-1-methylxanthine (IBMX; I5879, Sigma-Aldrich). HEK293T cells co-transfected with P_{Tight}-EGFP-*PGK*-rtTA and *3×CRE*-mCherry-PEST were treated with ATc and FSK at varying concentrations in the presence of 0.3 mM IBMX, according to the protocol as described in the figure panel. After incubation for 6–7 h at 37℃ with 5% CO_2, cells were lysed in cell extraction buffer supplemented with 1 mM PMSF and 1 × PIC following manufacturer's instructions, quantified using BCA protein assay (23225, Thermo Fisher Scientific), and stored in aliquots at -80℃ until use.

U87 and U937 cells seeded in 6-well plates were treated with 10% FBS for 10 min, 100 mM anisomycin (CS-4981, MedChem Express) for 1 h, or 20 mM H_2O_2 for 10 min, respectively. Then, cells were lysed in denaturing cell lysis buffer (6 M urea, 0.5% Triton X-100, 1 mM EDTA, 5 mM NaF in PBS, pH 7.2–7.4) supplemented with 1 × PIC and 2 × PPIC. After being lysed on ice for 15 min, samples were centrifuged at 2,000g for 5 min, and the supernatants were assayed immediately or stored at -80 ℃ until use. Cell lysates from three wells were pooled for each group. Before use, sample protein concentrations were measured using a BCA protein assay and equilibrated with the denaturing cell lysis buffer. Cell lysates were diluted 6-fold with dilution buffer (0.5% Triton X-100, 1 mM EDTA, 5 mM NaF in PBS, pH 7.2-7.4).

Serum sample collection

Human serum samples were collected from volunteers of laboratory workers and from individuals who undertook routine physical examinations for health screening in hospitals,

approved by the Human Research Ethics Committee of the Chinese Institute for Brain Research, Beijing.

Serum samples for anti-RBD IgG detection were collected in October 2021 from a cohort of 517 donors. The majority of these samples (n = 493) were collected from healthy individuals undergoing routine physical examinations during the initial phase of the SARS-CoV-2 vaccination campaign in Beijing, China. Due to privacy protection regulations, information regarding vaccination status and SARS-CoV-2 infection history (including infection status, vaccination status, vaccine type and manufacturer, number of doses received, and dates of administration) was not collected for these donors. To better validate the performance of BLISA, we obtained serum samples from additional 24 donors who voluntarily disclosed their SARS-CoV-2 vaccination records. Of these, 23 had received at least one dose of an inactivated SARS-CoV-2 vaccine, while one donor had neither been vaccinated nor tested positive for SARS-CoV-2 (the negative control).

Serum samples for HBV antigen detection were collected in June 2021 (cohort 1) and October 2023 (cohort 2) from donors undergoing routine physical examinations. Cohort 1 was collected from 529 donors, including 6 positive ($HBsAg^{+}HBeAg^{+}$) and 25 negative ($HBsAg^{-}HBeAg^{-}$) donors. Cohort 2 was collected from 600 donors, including 100 samples from donors that had been clinically diagnosed as HBV positive. Duplicate ELISA assays were conducted for 115 samples in cohort 1 and all samples in cohort 2. Only samples demonstrating reproducible results across both replicates were included in subsequent analyses.

BLISA on microplate surface

Detailed information about antibodies and the Nb-SS-DNA barcodes used are listed in **Supplementary Table 2**. HRP-conjugated secondary antibodies against rabbit IgG (1:30,000 diluted; 31460, Thermo Fisher Scientific) and against mouse IgG (1:30,000 diluted; 31430, Thermo Fisher Scientific) were used.

For cell lysate samples spiked in with purified GFP and mCherry, 50 μL purified proteins at a designated concentration were mixed with 1 μg/mL wildtype HEK293T cell lysate in coating buffer (50 mM carbonate buffer, pH 9.6). The mixtures were immobilized on a high-binding polystyrene microplate (449824, Thermo Fisher Scientific) for 2 h at 37°C. Coated microplates were washed three times with plate wash buffer (5 mM EDTA, 0.05% Tween-20 in PBS) and then blocked for 1 h at RT in 200 μL blocking buffer (0.05% Tween-20 in PFBB), followed by three additional wash steps using plate wash buffer. MaMBA-generated Ab-SS-DNA barcodes were pooled into incubation solution (blocking buffer supplemented with 5 mM EDTA, 0.4 mg/mL sheared Salmon sperm DNA, 2 μM TP1107-NGL-His_6 and 2 μM TP897-NGL-His_6). Samples were then incubated with the Ab-SS-DNA barcodes pool for 1 h at 37°C. Microplates were washed five times with plate wash buffer and three times with PBS containing 5 mM EDTA. 50 μL elution buffer (20 mM TCEP in PBS) was added to each well and incubated for 5–10 min at RT. Elution buffer containing retrieved DNAs was assayed immediately or stored at -20°C until analysis. 1 μL of elution buffer containing retrieved DNAs was used as a template for qPCR or sequencing library preparation. For ELISA experiments, samples were incubated with antibodies (diluted in PFBB) for 1 h at 37°C and washed three times with plate wash buffer, followed by incubation with HRP-conjugated secondary antibodies diluted in PFBB for 1 h at 37°C and washing five times with plate wash buffer. HRP-driven colorimetric readout was done by adding 50 μL TMB solution and incubating for 10 min at RT. 50 μL 1.8 N H_2SO_4 was

subsequently added to stop the reaction. Absorbance at 450 nm was measured immediately by microplate reader (Spark, Tecan). Values were corrected by subtracting the absorbance of blank wells. For cell lysate samples containing endogenously expressed GFP and mCherry, cell lysates were diluted to 1 μg/mL using coating buffer and immobilized on the microplate. Subsequent BLISA assays were conducted as described above.

For anti-RBD IgG detection in human serum samples, SARS-CoV-2 Spike RBD-His recombinant proteins (40592-V08B, Sino Biological) (1 μg/mL diluted in PBS) were immobilized on the microplate at RT overnight and washed three times with plate wash buffer using microplate washer (Wellwash™ Versa Microplate Washer, Thermo Fisher Scientific). After incubation in blocking buffer for 1 h at RT and three times of plate washing, a mixture of 1 μL serum sample and 49 μL PBS was added to the coated microplate and incubated for 1 h at 37°C. After five times of plate washing, captured anti-RBD IgGs were detected using Ab-SS-DNA barcodes (antibodies against human IgG in incubation buffer) for 1 h at 37°C. The plates were washed five times with plate wash buffer and three times with PBS containing 5 mM EDTA. DNA barcodes were retrieved using 50 μL elution buffer containing 10 pM normalization DNA oligos and incubated for 5–10 min at RT.

For HBsAg and HBeAg detection in human serum samples, 40 μL serum sample, 10 μL PBS, and 50 μL Ab-SS-DNA barcodes pool were mixed and added to microplates pre-coated with capture antibodies and incubated for 1 h at 37°C, followed by washing and DNA retrieval with 1 pM normalization DNA oligos.

BLISA on magnetic beads

Detailed information about the antibody pairs and the DNA barcodes are listed in **Supplementary Table 2**. 18 mg epoxy magnetic beads (Beijing Yunci Technology) were mixed with 0.1 M sodium phosphate (pH 7.4), capture antibodies (72–288 mg, corresponding to one vial of antibodies in the kit), and 1 M ammonium sulfate for 16–24 h at 37℃. Magnetic beads were then washed three times with PBS containing 1% Triton X-100, followed by blocking in PBS with 1% BSA and 0.05% Tween-20 for 2 h at RT. After magnetic isolation, antibody-coupled magnetic beads (10 mg/mL) were maintained in PBS with 0.1% BSA, 0.05% Tween-20, and 0.03% NaN_3 at 4℃. For multiplexing experiments, antibody-coupled beads for each target were mixed before use.

After washing twice with beads wash buffer (0.1% Triton X-100 in PBS), antibody-coupled magnetic beads were resuspended in wash buffer and aliquoted into a 96-well deep well plate (501102, NEST). Samples were then added and mixed with antibody-coupled magnetic beads for 30 min at RT using a plate mixer (800 rpm). Magnetic beads were isolated using a 96-well magnetic stand, followed by 3× wash steps with beads wash buffer. Antigen-captured beads were incubated with Ab-SS-DNA barcodes pool in beads incubation buffer (0.5% BSA, 0.05% Triton X-100, 0.1% dextran sulfate, 0.4 mg/mL sheared Salmon sperm DNA, 5 μM TP1107-NGL-His_6, 2 μM TP897-NGL-His_6 in PBS) for 30 min at RT using a plate mixer (800 rpm), followed by 5× wash steps with beads wash buffer. Beads were rinsed twice with PBS, and DNA barcodes were retrieved using 50 μL elution buffer (20 mM TCEP in PBS) for 5–10 min at RT using a plate mixer (1000 rpm). After magnetic isolation, solutions containing retrieved DNAs were transferred to new tubes and measured immediately or stored at -20℃ until analysis.

Quantitative PCR (qPCR)

One microliter of solutions containing retrieved DNAs was used for qPCR (triplicates for each sample; 20 μL reaction volume, SYBR qPCR master mix, Q712, Vazyme) using a CFX 96 machine (Bio-rad). Primer sequences are listed in **Supplementary Table 5**.

Sequencing library preparation

For the two-step PCR protocol (**Extended Data Fig. 9**), a 25 μL PCR to add well-specific barcode was performed for each sample using 1 μL retrieved DNA barcodes, 0.1 mM dNTPs, 0.5 U Q5 high-fidelity DNA polymerases (NEB), 1× Q5 reaction buffer, 0.4 μM well-specific forward primers, and 0.4 μM reverse primers (**Supplementary Table 6**). Retrieved DNA barcodes were amplified over 9 cycles of 98°C for 10 s, 50°C for 30 s, and 72°C for 10 s. For each microplate, 1 μL PCR product from each well were pooled and subsequently purified using 1.8× AMPure XP beads (Beckman Coulter), followed by elution using 30 μL nuclease-free water. Additional 50 μL PCR for each microplate to add sequencing adaptors was performed using 29 μL purified pooled PCR products, 0.2 mM dNTPs, 1 U Q5 polymerase, 1× Q5 reaction buffer, 0.5 μM adaptor forward primer and 0.5 μM adaptor reverse primer containing i7 index. Well-barcoded DNAs were amplified over 9 cycles of 98°C for 10 s, 50°C for 30 s, and 72°C for 10 s. PCR products were purified using 1.8× AMPure XP beads. Final sequencing libraries were eluted in 30 μL nuclease-free water.

For the three-step PCR protocol with phasing spacers addition (Extended Data Fig. 11), a 25 μL PCR to add well-specific barcode was performed for each sample using 1 μL retrieved DNA barcodes, 0.1 mM dNTPs, 0.5 U Q5 polymerases, 1× Q5 reaction buffer, 0.4 μM well-specific forward primers, and 0.4 μM reverse primers (**Supplementary Table 6**). Retrieved DNA barcodes were amplified over 9 cycles of 98°C for 10 s, 50°C for 30 s, and 72°C for 10 s.

For each microplate, 0.73 μL PCR product from each well were pooled and purified using 1.8× AMPure XP beads, followed by elution using 85 μL nuclease-free water. Eight 25 μL PCRs were performed to add phasing spacers using 10 μL purified pooled PCR products, 0.1 mM dNTPs, 0.5 U Q5 polymerases, 1× Q5 reaction buffer, 0.4 μM PS forward primers, and 0.4 μM PS reverse primers (**Supplementary Table 6**). Well-barcoded DNAs were amplified over 9 cycles of 98°C for 10 s, 55°C for 30 s, and 72°C for 10 s. PCR products (8.75 μL of each reaction) were pooled and purified using 1.8× AMPure XP beads, followed by elution using 30 μL nuclease-free water. A final 50 μL PCR was performed to add sequencing adaptors using 5 μL phasing spacer added DNAs, 0.2 mM dNTPs, 0.5 U Q5 polymerases, 1× Q5 reaction buffer, 0.5 μM forward primers, and 0.5 μM reverse primers containing i7 index (plate index). NGS libraries were amplified over 4 cycles of 98°C for 10 s, 60°C for 30 s, and 72°C for 10 s. NGS libraries were then purified using 1.8× AMPure XP beads and eluted with 20 μL nuclease-free water. NGS libraries for each microplate were individually analyzed and quantified before pooling. NGS Sequencing was performed on a HiSeq2500 System (Illumina).

NGS data analysis

We devised a Snakemake[58] pipeline to extract and quantify well barcode (well-bc), antibody-specific barcode (Ab-bc), and unique molecular identifiers (UMI) from the BLISA libraries.

For standard BLISA libraries, whitelists for well-bc, Ab-bc, and UMIs were generated at positions 1–6, 21–26, and 27–41, respectively, from the sequencing reads, using the “whitelist” command from UMI-tools[59]. The whitelist was filtered with respect to a ground truth list, and the well-bc, Ab-bc, and UMIs were extracted using the “extract” command. For BLISA libraries

with staggered sequences, two anchor sequences “GACAAGTGGCCACAAACCACCAG” and “CTTGTGGAAAGGACGAAACA” located between the well-bc, Ab-bc, and UMIs were used to identify and extract the barcodes and UMIs using Biopython[60].

Base pair corrections were performed on barcode-UMI combinations 2 Hamming Distance from the ground truth barcode-UMI combinations as initially designed in the experiments.

The extracted barcodes and UMIs were demultiplexed and aggregated into dataframes. Analyses and visualization were performed using tidyverse[61].

Statistics and reproducibility

Statistical significance was evaluated using Prism 9 (GraphPad). All fluorescence intensity, immunostaining, BLISA qPCR, Western blot, and ELISA experiments were independently performed ≥ 3 times with similar results. HTS-based BLISA experiments were performed once.

Data and codes availability

The raw sequence data reported in this paper have been deposited in the Genome Sequence Archive (Genomics, Proteomics & Bioinformatics 2021) in National Genomics Data Center (Nucleic Acids Res 2022), China National Center for Bioinformation / Beijing Institute of Genomics, Chinese Academy of Sciences under the accession GSA: CRA012054, that are publicly accessible at https://ngdc.cncb.ac.cn/gsa.

The raw images generated in this study are not suitable for distribution through public repositories due to the large file size and are available from the corresponding authors upon request.

The code for BLISA analysis is available at https://github.com/RuiyuRayWang/BLISAcounts.

Acknowledgments

We thank Dr. Ting Chen (NIBS, Beijing, China) for her supports in the experiments on human skin samples. The reagents for anti-RBD IgG and HBV antigens detection experiments were supported by Beijing Wantai Biological Pharmacy, Peking University International Hospital, and Beijing Tiantan Hospital. Cartoon illustrations are generated at BioRender.com. We thank all members of R.L.'s lab and M.L.'s lab for their assistance in this study. R.L. is supported by National Natural Science Foundation of China (32322032), China Brain Initiative Grant (2022ZD0206700), Beijing Nova Program (20230484303), and the Beijing Municipal Government. M.L. is supported by China Brain Initiative Grant (STI2030-Major Projects 2021ZD0202803), the Research Unit of Medical Neurobiology at Chinese Academy of Medical Sciences (2019RU003), New Cornerstone Investigator Program, and the Beijing Municipal

Government. The funders had no role in the study design, data collection and analysis, manuscript preparation, or decision to publish the manuscript.

Author contributions

R.L., S.Z., and M.L. designed the experiments. S.Z. performed most of the experiments. R.W. performed the sequencing analysis. X.G. and Q.G. set up the imaging platform and helped with image processing. S.Z., R.L., and M.L. wrote the manuscript with contributions from all other authors.

Competing interests

The National Institute of Biological Sciences (NIBS), Beijing, China has filed patent applications related to this work with R.L., S.Z., and M.L. listed as inventors. All other authors have no competing interests.

Figure Legends

Fig. 1. Development and application of MaMBA and *mis*HCR. a, Schematics of the DNA oligo-conjugated nanobody production process. **b**, Coomassie stained SDS-PAGE gel of purified nanobody (Nb-NGL-His_6), *Oa*AEP1 reaction product (Nb-NGV-N_3), and click reaction products (Nb-DNA oligo). **c**, MaMBA workflow. IgG antibodies are separately incubated with DNA oligo-conjugated nanobodies bearing unique DNA barcodes, forming antibody-Nb-DNA oligo complexes (Ab-Nb 1 to Ab-Nb 3). These complexes are subsequently purified using ultra centrifugal filters or IgG-conjugated beads, pooled, and applied to various assays. **d**, Fluorescence confocal images of human psoriatic skin section stained for DAPI and six antigens by three rounds of *mis*HCR. IgG types of the employed antibodies are indicated in parentheses. Scale bar, 300 μm. Rb, rabbit; Mus, mouse; Th, tyrosine hydroxylase; PDGFRα, platelet-derived growth factor receptor A; KRT14, keratin 14; DCT, dopachrome tautomerase; αSMA, alpha-smooth muscle actin.

Fig. 2. Multi-round immunostaining using *mis*HCR^n. a, Schematics of the production process for cleavable DNA oligo-conjugated nanobodies. **b**, Workflow of *mis*HCR^n staining and imaging. The process begins with the first round of staining (1st round of *mis*HCR), where a pool of primary antibodies barcoded with orthogonal cleavable HCR initiators (Ab-SS-i1 to Ab-SS-in) is applied to the sample simultaneously. This is followed by sequential rounds of HCR imaging (image rounds). Upon completion of the image rounds, HCR initiators are removed using TCEP to cleave the disulfide bonds, enabling the start of the second round of staining (2nd round of *mis*HCR). Antibodies used in the 2nd round of *mis*HCR can be equipped with the same set of HCR initiators as in the 1st round of *mis*HCR (Ab-SS-i1' to Ab-SS-in'). This process can be iteratively performed for multi-round *mis*HCR. **c**, Fluorescence confocal images of the DRN in a mouse brain section, stained for 12 antigens by *mis*HCR^2 and counterstained with DAPI. The imaging location is highlighted in the red boxed region of the mouse brain atlas shown at the bottom left. IgG types of the employed antibodies are indicated in parentheses. Scale bar, 100

μm. **d**, Zoomed-in views of the region marked by a dotted-box in panel **c**. Arrows indicate three cell types (1, $Ddc^{+}Th^{+}Tph2^{-}$ cells; 2, $Ddc^{+}Th^{-}Tph2^{+}$ cells; 3, $Ddc^{+}Th^{-}Tph2^{-}5\text{-}HT^{-}$ cells). Scale bar, 50 μm. nNOS, neuronal nitric oxide synthase; GFAP, glial fibrillary acidic protein; NF-H, neurofilament-H; Tph2, tryptophan hydroxylase 2; GABA, gamma-aminobutyric acid; Tmem119, transmembrane protein 119; Ddc, dopa decarboxylase; 5-HT, 5-hydroxytryptamine; Iba1, ionized calcium binding adaptor molecule.

Fig. 3. Barcode-linked immunosorbent assay (BLISA). a, Workflow of direct antigen detection using BLISA. **b**, Schematics of multiplexed detection for GFP, mCherry, and α-tubulin using BLISA. **c**, Quantification of spiked-in purified GFP, spiked-in purified mCherry, and endogenous α-tubulin in cell lysates using qPCR-based BLISA. Negative control (NC) represents cell lysates without spiked-in proteins. ΔCt values are normalized to the NC group, where $\Delta Ct\ (NC=1) = Ct_{NC}-Ct_{Target}+1$. The dose-response curves for purified GFP (green) and mCherry (red) are fitted using a five-parameter logistic (5PL) function. n = 3 replicates; mean±s.e.m.. **d**, Schematics of two drug-inducible gene expression systems for expressing GFP and mCherry in HEK293T cells. **e**, Western blot of cell samples treated with varying concentrations of ATc and FSK. **f**, Pearson's correlation between BLISA and Western blot results for measuring relative expression levels (REL, normalized to α-tubulin) of GFP (left) and mCherry (right). $REL=2^{-(CtGFP/mCherry-Ct\alpha\text{-}tubulin)}$. ATc, anhydrotetracycline hydrochloride; FSK, forskolin.

Fig. 4. Magnetic bead-based BLISA for multiplexed detection. a, Workflow of the magnetic bead-based BLISA. **d**, Comparison of 7-plex BLISA (left) and ELISA (middle) for detecting the

phosphorylation of seven endogenous proteins in U87 and U937 cells under various culture conditions. The right panel shows Pearson's correlation coefficients between BLISA and ELISA results for each target protein. *n* = 3 replicates; mean±s.e.m.. **e**, Heatmap showing average Z-scores of the phosphorylation levels of seven proteins in U87 cells following different drug treatments. *n* = 2 biological replicates. **d**, ELISA quantification of phosphorylation levels for seven proteins in U87 cells. n = 3 biological replicates; two-sided t-tests. p-p38α, phospho-p38α (T180/Y182); p-ERK1/2, phospho-ERK1 (T202/Y204)/ERK2 (T185/Y187); p-JNK, phospho-JNK (Pan Specific); p-AMPKα1, phospho-AMPKα1 (T183); p-CREB, phospho-CREB (S133); p-Src, phospho-Src (Y419); p-Akt, phospho-Akt (S473); NT, non-treated; FBS, fetal bovine serum; Aniso, anisomycin.

Fig. 5. HTS-based BLISA for high-throughput detection of IgGs in human serum samples. **a**, Workflow of sandwich immunoassay-based IgG detection using BLISA. **b**, Pearson's correlation between results from two technical duplicate. Red dots represent negative samples. **c**–**d**, Quantification of anti-RBD IgG levels in twelve samples from vaccinated donors using HTS-based BLISA (**c**) and ELISA (**d**). **f**, Pearson's correlation between BLISA and ELISA results shown in (**c)** and (**d**). *n* = 2 replicates; mean±s.e.m.. **f**, Distribution of normalized IgG abundance in negative and test samples (*n* = 493). Red dots represent negative samples. The solid grey line indicates the mean normalized abundance of negative samples. The dotted grey line represents the mean plus three standard deviations (mean+3SD).

Fig. 6. HTS-based BLISA for high-throughput simultaneous detection of two HBV antigens in human serum samples. **a**, Workflow of sandwich immunoassay-based HBV antigen

detection using BLISA. **b**–**c**, Sensitivity and specificity of two-plex BLISA for detecting HBsAg. *n*=462 ELISA-negative samples and 119 ELISA-positive samples from cohort 2. **d**–**e**, Sensitivity and specificity of two-plex BLISA on detecting HBeAg. *n*=505 ELISA-negative samples and 90 ELISA-positive samples from cohort 2. Solid grey lines indicate the mean normalized abundance of ELISA-confirmed negative samples. Dotted grey lines represent the mean+3 standard deviations (mean+3SD). **f**, Pearson's correlation between technical duplicates for HBsAg (upper) and HBeAg (bottom) measurements in serum samples from cohort 2 (*n*= 600).

Extended Data Figure Legends

Extended Data Fig. 1. Characterization of *mis*HCR. a, Schematics of *is*HCR and *mis*HCR procedures. **b**–**d**, Fluorescence confocal images of mouse brain sections stained using *mis*HCR or conventional fluorescent immunohistochemistry with fluorophore-conjugated nanobodies. n = 3 brain sections for each group; mean±s.e.m.; two-sided unpaired t-test. Scale bar, 100 μm. **e**, Fluorescence confocal images of HeLa cells stained against α-tubulin using a conventional method with a fluorophore-conjugated secondary antibody (2nd Ab) (left) or *mis*HCR (right). Insets show zoomed-in views of the boxed region. Scale bar, 10 μm. Bottom panel shows representative intensity profiles along straight lines drawn perpendicular to microtubule structures. **f**, Quantification of full width at half maximum (FWHM) derived from intensity profiles along a straight line drawn perpendicular to microtubule structure stained using traditional immunohistochemistry (2nd Ab) or *mis*HCR. n = 26 for 2nd Ab and 25 for *mis*HCR; mean±s.e.m.; two-sided unpaired t-test.

Extended Data Fig. 2. Efficient and reproducible HCR signal removal by formamide treatment. a, Workflow of *mis*HCR imaging. Pooled antibodies (Ab-i1 to Ab-in), each conjugated with distinct HCR initiators, are applied simultaneously for antigen (Ag. 1 to Ag. n) detection. Subsequently, sequential rounds of imaging are performed via hybridization and dehybridization of orthogonal HCR amplifier pairs (Amp.). **b**, Fluorescence confocal images of mouse brain sections before and after HCR amplifiers removal using formamide. Scale bar, 500 μm. **c**, Fluorescence confocal images of the DRN in mouse brain sections stained against NeuN and NF-H through five consecutive cycles of HCR amplification/formamide treatment. Scale bar, 100 μm. **d**, Quantification of mean fluorescence intensity for NeuN (left) and NF-H (right) after

each round of HCR amplification. Images of each group were acquired using identical microscopy settings. n = 3 brain sections for each group; mean±s.e.m.; Dunn's multiple comparison tests.

Extended Data Fig. 3. *Mis*HCR imaging of human psoriatic and healthy skin sections. Fluorescence confocal images of skin sections from a patient with psoriasis (up) and a healthy donor (bottom) stained against six antigens. The psoriatic skin sample corresponds to that shown in **Fig. 1d**. Dotted lines and arrows indicate pathological features characteristic of psoriatic skins. Scale bar, 300 μm.

Extended Data Fig. 4. Efficient *mis*HCR signal removal by TECP treatment. Fluorescence confocal images of mouse brain sections before and after TCEP treatment to remove HCR amplifiers and initiators. The target molecules were MAP2, Ddc, and nNOS for the first round; NeuN, Iba1, and GFAP for the second round; Th, and NF-H for the third round. Scale bar, 300 μm. MAP2, microtubule-associated protein 2.

Extended Data Fig. 5. *mis*HCR^{n} for immunostaining nine target antigens using three orthogonal HCR initiators. a, Fluorescence confocal images of mouse brain sections stained against nine targets by three rounds of *mis*HCR. The red-boxed region of the mouse brain atlas shown in the bottom right indicates the imaging location. Scale bar, 300 μm. **b**, Zoomed-in views of the dotted-box region marked in **a**. Scale bar, 25 μm.

Extended Data Fig. 6. Validation of the specificity of *mis*HCR. Mouse brain sections were immunostained with primary antibodies against different antigens, followed by and simultaneous incubation with equal amounts of fluorophore-conjugated secondary antibodies (2nd Ab) and Nb-HCR initiators (*mis*HCR). Scale bar, 100 μm.

Extended Data Fig. 7. BLISA for detecting proteins endogenously expressed in cells. a, Schematics of the tetracycline-regulated gene expression system for driving GFP expression. **b**, Western blot of cell samples treated with varying concentrations of ATc. **c**, Pearson's correlations between qPCR-based BLISA and Western blot results for measuring relative expression level (REL, normalized to α-tubulin) of GFP. $REL=2^{-(CtGFP-Ct\alpha\text{-}tubulin)}$. **d**, Schematics of the cAMP response element-mediated gene expression system for driving mCherry expression. **e**, Western blot of cell samples treated with varying concentrations of FSK. **f**, Pearson's correlations between qPCR-based BLISA and Western blot results for measuring REL (normalized to α-tubulin) of mCherry. $REL=2^{-(CtmCherry-Ct\alpha\text{-}tubulin)}$.

Extended Data Fig. 8. Comparative analysis of standard curves for magnetic bead-based BLISA and ELISA. a, Dose-response curves for seven purified phosphorylated proteins quantified using BLISA (qPCR, ΔCt) and ELISA (Absorbance). Curves were fitted using 4PL or 5PL functions. Limit of detection (LOD) was defined as the mean signal of the blank group plus three standard deviations. **b**, R^2 for the standard curves shown in panel **a**. **c**, Multiplexed detection of seven purified phosphorylated proteins using magnetic bead-based BLISA. n = 3 replicates; mean±s.e.m..

Extended Data Fig. 9. Validation of HTS-based BLISA. a, Schematics of DNA barcode design and amplicon generation for BLISA sequencing. Released DNA barcodes undergo a two-step PCR protocol for well barcode (well-bc) addition and Illumina sequencing adaptors tagging. **b**, UMI counts for three target proteins (GFP, mCherry, and α-tubulin) in cell lysates spiked in with varying concentrations of GFP and mCherry. *n* = 3 replicates; mean±s.e.m.. **c**, Dose-response curves for the GFP (upper) and mCherry (bottom) fitted using a 5PL function. n=3 replicates; mean±s.e.m..

Extended Data Fig. 10. Comparative analysis of the sensitivity of BLISA and ELISA for human IgG detection. a, Schematics of ELISA (left) and BLISA (right) for human IgG detection. **b**, Dose-response curves for human IgG detection by BLISA and ELISA fitted using a 5PL function. The dynamic ranges of ELISA (blue) and BLISA (red) are indicated by dashed lines, spanning from the limit of quantification (LOQ) to the lower limit of 95% confidence interval. *n* = 3 replicates; mean±s.e.m.. **c**, Pearson's correlation between qPCR-based BLISA and ELISA results for anti-RBD IgG detection. The red dot represents the negative sample.

Extended Data Fig. 11. Sequencing library preparation for BLISA. a, Schematics of sequencing amplicon generation procedure. **b**, Annotated amplicon sequence of BLISA for Illumina sequencing.

Extended Data Fig. 12. Quantification of anti-RBD IgG in human serum samples using HTS-based BLISA. a, Comparison of coefficient of variation (CV) between duplicates for raw (grey) and normalized (red) data. Histogram shows relative distributions of CV between

duplicates. Box plots show median, interquartile range, and whiskers extending to the minimum and maximum. Two-sided paired t-test. **b**, Frequency distribution of normalized anti-RBD IgG abundances of test samples across assay plates. **c**, Scatter plot of normalized anti-RBD IgG abundances of individual serum samples (*n*=517) quantified using HTS-based BLISA. Each plate includes a negative control sample in duplicates.

Supplementary Figure Legends

Supplementary Fig. 1. Efficiency assessment of nanobody-DNA oligo conjugation. a, Coomassie-stained reducing SDS-PAGE gel of protein products at each step of OaAEP1-mediated azide functional groups addition to nanobodies. The purified nanobody (*i.e.*, input) was incubated with OaAPE1 and azide-bearing substrate peptides (*i.e.*, Nb reaction mixture). After reaction, the products (*i.e.*, Nb-NGV-N_3) were purified by Ni-NTA agarose beads to remove unreacted His_6-tagged nanobody (*i.e.*, After Ni-NTA). The excess substrate peptides were further depleted using desalting columns (*i.e.*, After desalting). **b**, Quantification of OaAPE1-mediated reaction yields, determined by densitometric measurement of Nb-NGV-N_3 band intensities. **c**, Coomassie-stained reducing SDS-PAGE gel of Nb-NGV-N_3 and nanobodies conjugated with DNA oligo of different lengths (*i.e.*, Nb-oligo (62bp) and Nb-oligo (42bp)). **d**, Quantification of DNA conjugation yields, determined by densitometric measurement of band intensities corresponding to nanobody-DNA conjugates.

Supplementary Fig. 2. Comparison of antibody-DNA oligo labeling methods. a, Schematics of non-site-specific labeling methods for generating DNA oligo-conjugated antibodies with increased labeling degree. **b**, Silver-stained reducing SDS-PAGE gel of antibodies conjugated with 62bp DNA oligos using the amine-based method (Thunder-link antibody labeling kit) at various antibody:DNA ratios. **c**, Silver-stained reducing SDS-PAGE gel of antibodies conjugated with 62bp DNA oligos using the thiol-based method (thiol-maleimide reaction) at various antibody:DNA ratios. **d**, Western Blot of DNA oligo-labeled antibodies generated by MaMBA strategy using different antibody:nanobody-DNA oligo (Nb-oligo) ratios. Samples were separated by native PAGE and transferred to PVDF membrane for Western Blot. DNA oligos

were 3'-biotin modified and detected using streptavidin. **e**, Western Blot of HEK 293T cell lysates with or without EGFP expression using different DNA oligo-labeled antibodies. The concentrations of anti-GFP antibodies were identical for each group. DNA oligos were 3'-biotin modified and detected using streptavidin. All groups were chemiluminescently detected simultaneously. Endogenous biotinylated carboxylases in cell lysates served as loading controls.

Supplementary Fig. 3. HTS-based BLISA for high-throughput detection of two HBV antigens in serum samples from cohort 1. a, Scatter plot of normalized HBsAg and HBeAg abundances of individual serum samples (*n*= 529) quantified using HTS-based 2-plex BLISA. **b**, Frequency distributions of normalized HBsAg (blue) and HBeAg (red) abundances of test samples. **c**, Pearson's correlation between technical duplicates for HBsAg (left) and HBeAg (right) measurements. **d**, HBsAg and HBeAg levels of control samples in cohort 1 measured by HTS-based BLISA. Histogram of normalized HBsAg and HBeAg abundances in negative ($HBsAg^{-}HBeAg^{-}$) and positive ($HBsAg^{+}HBeAg^{+}$) control groups were quantified using HTS-based BLISA. n = 25 for $HBsAg^{-}HBeAg^{-}$ and 6 for $HBsAg^{+}HBeAg^{+}$; mean±s.e.m.; Two-sided unpaired t-tests. **e**–**f**, Sensitivity and specificity of two-plex BLISA for detecting HBsAg. *n*=87 ELISA-negative samples and 28 ELISA-positive samples from cohort 1. **g**–**h**, Sensitivity and specificity of two-plex BLISA for detecting HBeAg. *n*=108 ELISA-negative samples and 7 ELISA-positive samples from cohort 1. Solid grey lines indicate the mean normalized abundance of ELISA-confirmed negative samples. Dotted grey lines represent the mean+3 standard deviations (mean+3SD).

Supplementary Fig. 4. Performance evaluation of two-plex BLISA for detecting HBV antigens using ELISA-independent thresholds. a–**b**, Sensitivity and specificity of two-plex BLISA for detecting HBsAg (**a**) and HBeAg (**b**) in serum samples from cohort 1. Solid grey lines indicate the mean normalized abundance of test samples (mean.t; *n*=529). Dotted grey lines represent the mean+standard deviations (mean.t+SD.t). **c**–**d**, Sensitivity and specificity of two-plex BLISA for detecting HBsAg (**c**) and HBeAg (**d**) in serum samples from cohort 2. Solid grey lines indicate the mean normalized abundance of test samples (mean.t; *n*=500). Dotted grey lines represent the mean+standard deviations (mean.t+SD.t).

Supplementary Fig. 5. Comparison of the amine-based, thiol-based, and MaMBA-based antibody labeling methods.

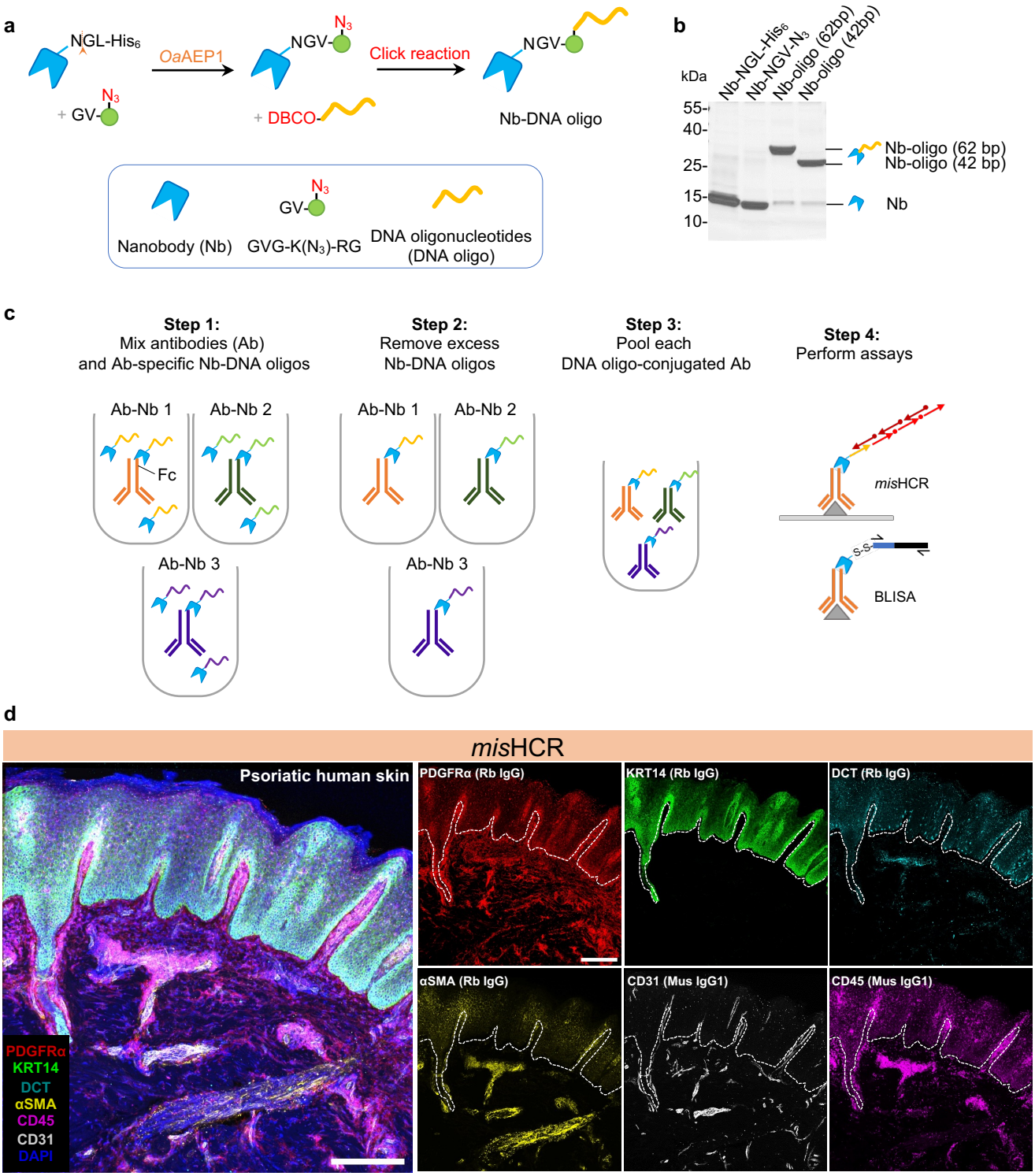

Fig. 1. Development and application of MaMBA and *mis*HCR. a, Schematics of the DNA oligo-conjugated nanobody production process. **b**, Coomassie stained SDS-PAGE gel of purified nanobody (Nb-NGL-His$_6$), *Oa*AEP1 reaction product (Nb-NGV-N$_3$), and click reaction products (Nb-DNA oligo). **c**, MaMBA workflow. IgG antibodies are separately incubated with DNA oligo-conjugated nanobodies bearing unique DNA barcodes, forming antibody-Nb-DNA oligo complexes (Ab-Nb 1 to Ab-Nb 3). These complexes are subsequently purified using ultra centrifugal filters or IgG-conjugated beads, pooled, and applied to various assays. **d**, Fluorescence confocal images of human psoriatic skin section stained for DAPI and six antigens by three rounds of *mis*HCR. IgG types of the employed antibodies are indicated in parentheses. Scale bar, 300 μm. Rb, rabbit; Mus, mouse; Th, tyrosine hydroxylase; PDGFRα, platelet-derived growth factor receptor A; KRT14, keratin 14; DCT, dopachrome tautomerase; αSMA, alpha-smooth muscle actin.

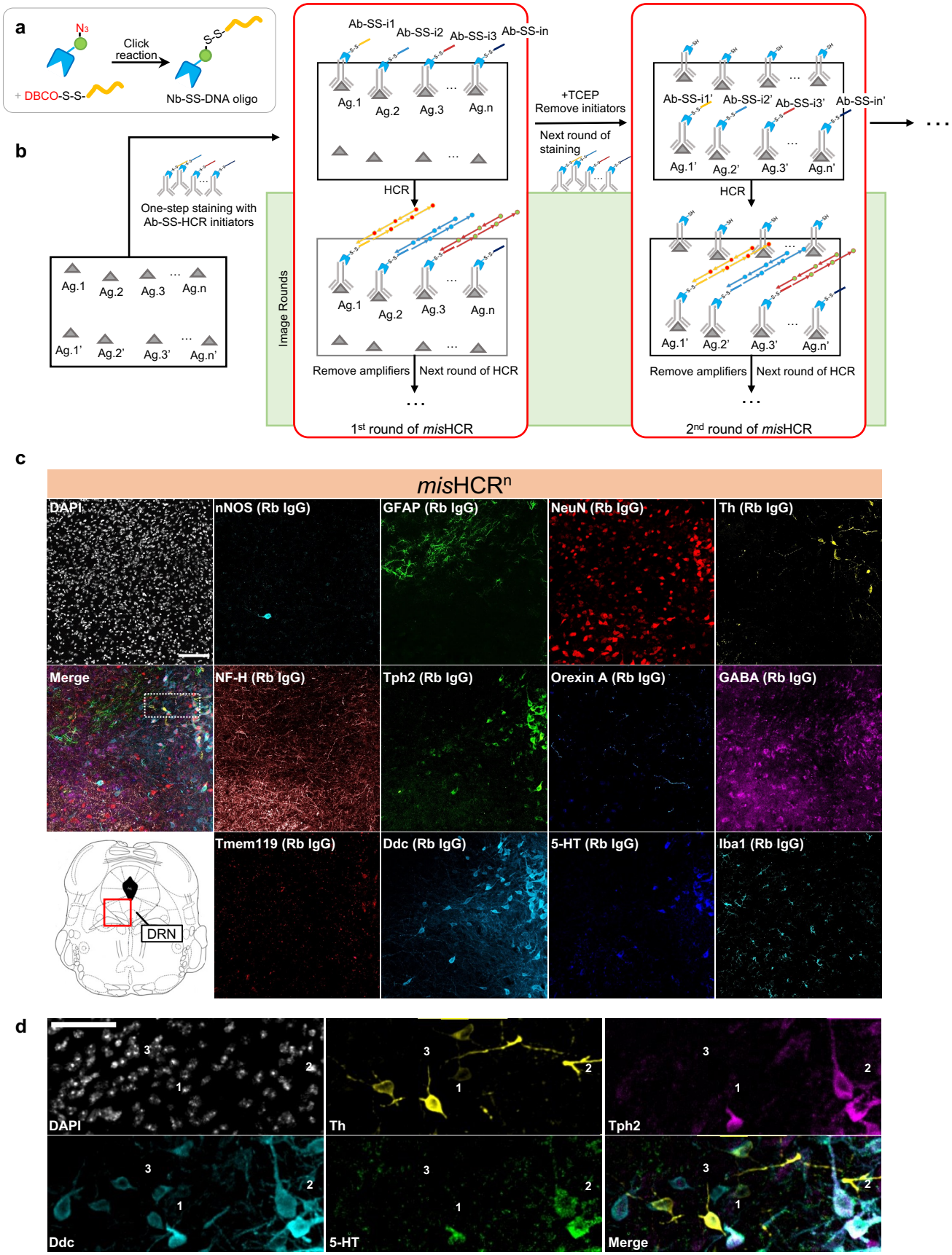

Fig. 2. See next page for caption.

Fig. 2. Multi-round immunostaining using *mis*HCR^n. a, Schematics of the production process for cleavable DNA oligo-conjugated nanobodies. **b**, Workflow of *mis*HCR^n staining and imaging. The process begins with the first round of staining (1st round of *mis*HCR), where a pool of primary antibodies barcoded with orthogonal cleavable HCR initiators (Ab-SS-i1 to Ab-SS-in) is applied to the sample simultaneously. This is followed by sequential rounds of HCR imaging (image rounds). Upon completion of the image rounds, HCR initiators are removed using TCEP to cleave the disulfide bonds, enabling the start of the second round of staining (2nd round of *mis*HCR). Antibodies used in the 2nd round of *mis*HCR can be equipped with the same set of HCR initiators as in the 1st round of *mis*HCR (Ab-SS-i1' to Ab-SS-in'). This process can be iteratively performed for multi-round *mis*HCR. **c**, Fluorescence confocal images of the DRN in a mouse brain section, stained for 12 antigens by *mis*HCR^2 and counterstained with DAPI. The imaging location is highlighted in the red boxed region of the mouse brain atlas shown in the bottom left. IgG types of the employed antibodies are indicated in parentheses. Scale bar, 100 μm. **d**, Zoomed-in views of the region marked by a dotted-box in panel **c**. Arrows indicate three cells types (1, Ddc$^+$Th$^+$Tph2$^-$ cells; 2, Ddc$^+$Th$^-$Tph2$^+$ cells; 3, Ddc$^+$Th$^-$Tph2$^-$5-HT$^-$ cells). Scale bar, 50 μm. nNOS, neuronal nitric oxide synthase; GFAP, glial fibrillary acidic protein; NF-H, neurofilament-H; Tph2, tryptophan hydroxylase 2; GABA, gamma-aminobutyric acid; Tmem119, transmembrane protein 119; Ddc, dopa decarboxylase; 5-HT, 5-hydroxytryptamine; Iba1, ionized calcium binding adaptor molecule.

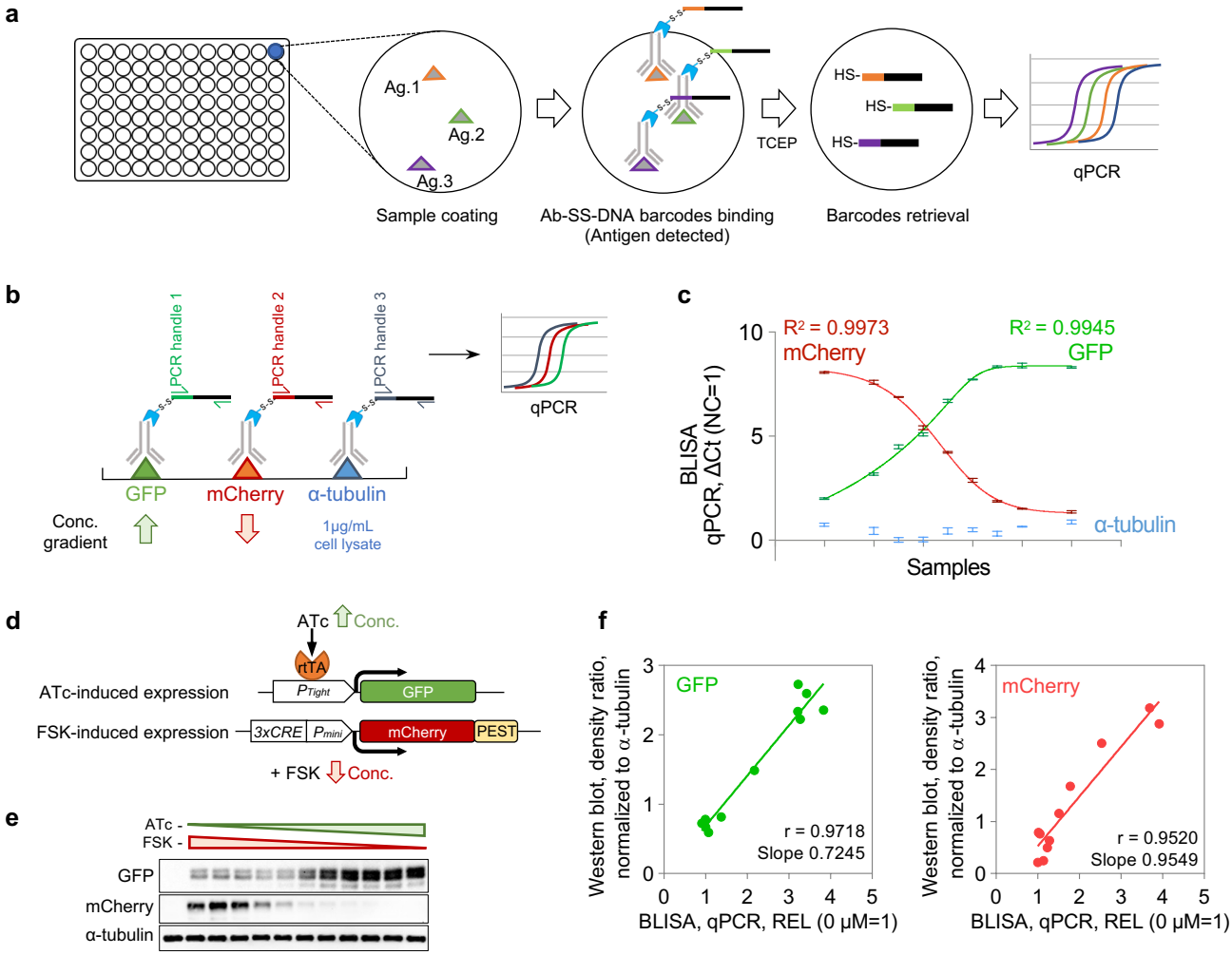

Fig. 3. Barcode-linked immunosorbent assay (BLISA). a, Workflow of direct antigen detection using BLISA. **b**, Schematics of multiplexed detection for GFP, mCherry, and α-tubulin using BLISA. **c**, Quantification of spiked-in purified GFP, spiked-in purified mCherry, and endogenous α-tubulin in cell lysates using qPCR-based BLISA. Negative control (NC) represents cell lysates without spiked-in proteins. ΔCt values are normalized to the NC group, where ΔCt (NC=1) = Ct_{NC}-Ct_{Target}+1. The dose-response curves for purified GFP (green) and mCherry (red) are fitted using a five-parameter logistic (5PL) function. n = 3 replicates; mean±s.e.m.. **d**, Schematics of two drug-inducible gene expression systems for expressing GFP and mCherry in HEK293T cells. **e**, Western blot of cell samples treated with varying concentrations of ATc and FSK. **f**, Pearson's correlation between BLISA and Western blot results for measuring relative expression levels (REL, normalized to α-tubulin) of GFP (left) and mCherry (right). REL=$2^{-(CtGFP/mCherry-Ct\alpha\text{-}tubulin)}$. ATc, anhydrotetracycline hydrochloride; FSK, forskolin.

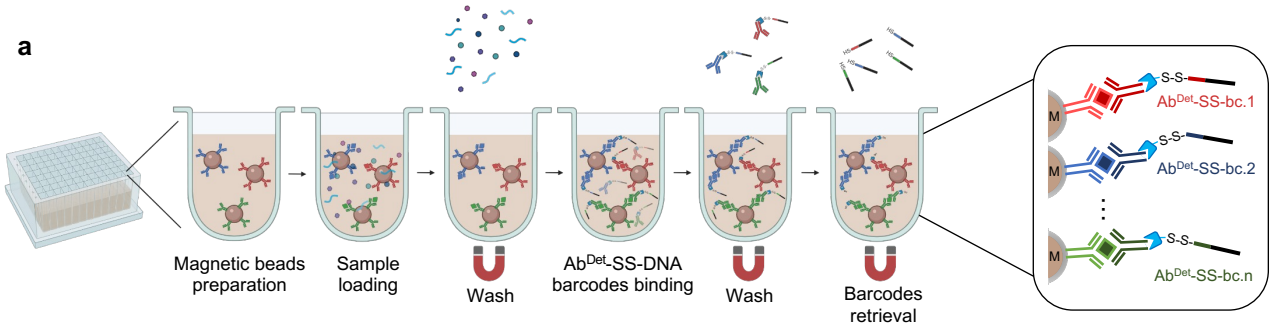

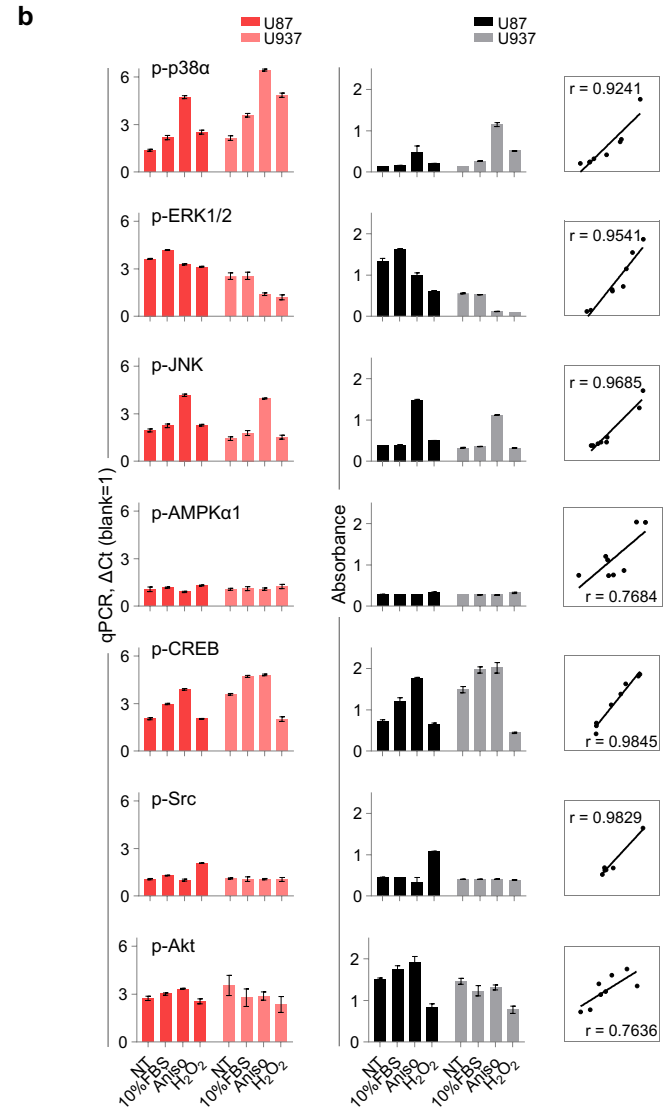

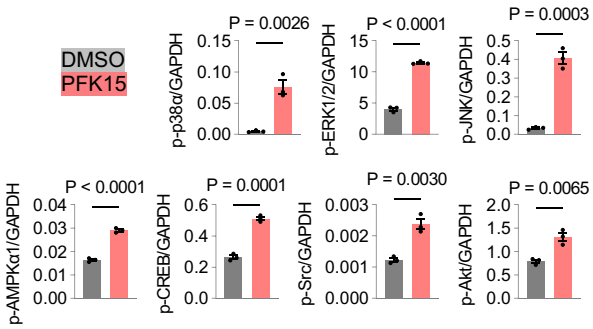

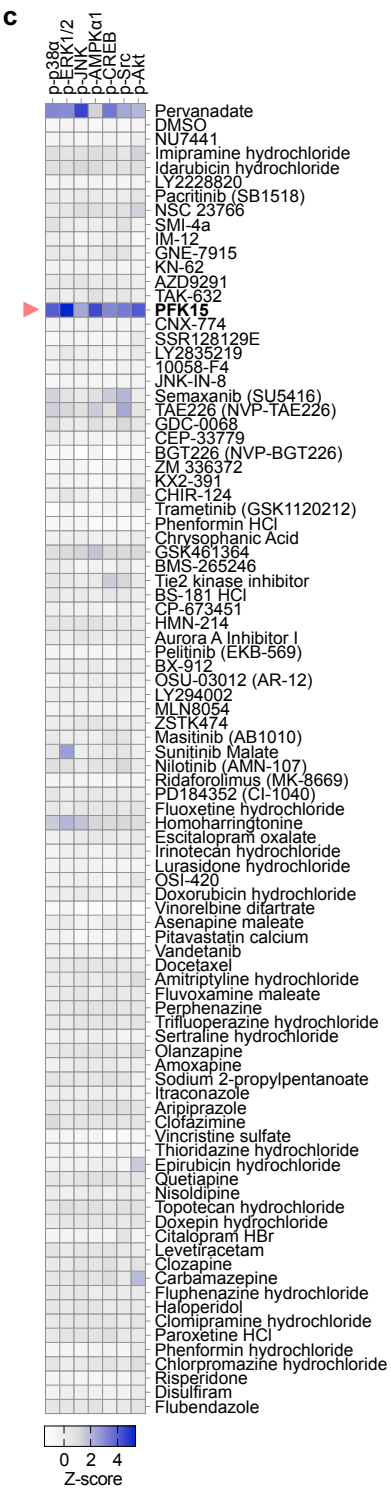

Fig. 4. See next page for caption.

Fig. 4. Magnetic bead-based BLISA for multiplexed detection. a, Workflow of the magnetic bead-based BLISA. **b**, Comparison of 7-plex BLISA (left) and ELISA (middle) for detecting the phosphorylation of seven endogenous proteins in U87 and U937 cells under various culture conditions. The right panel shows Pearson's correlation coefficients between BLISA and ELISA results for each target protein. n = 3 replicates; mean±s.e.m.. **c**, Heatmap showing average Z-scores of the phosphorylation levels of seven proteins in U87 cells following different drug treatments. n = 2 biological replicates. **d**, ELISA quantification of phosphorylation levels for seven proteins in U87 cells. n = 3 biological replicates; two-sided t-tests. p-p38α, phospho-p38α (T180/Y182); p-ERK1/2, phospho-ERK1 (T202/Y204)/ERK2 (T185/Y187); p-JNK, phospho-JNK (Pan Specific); p-AMPKα1, phospho-AMPKα1 (T183); p-CREB, phospho-CREB (S133); p-Src, phospho-Src (Y419); p-Akt, phospho-Akt (S473); NT, non-treated; FBS, fetal bovine serum; Aniso, anisomycin.

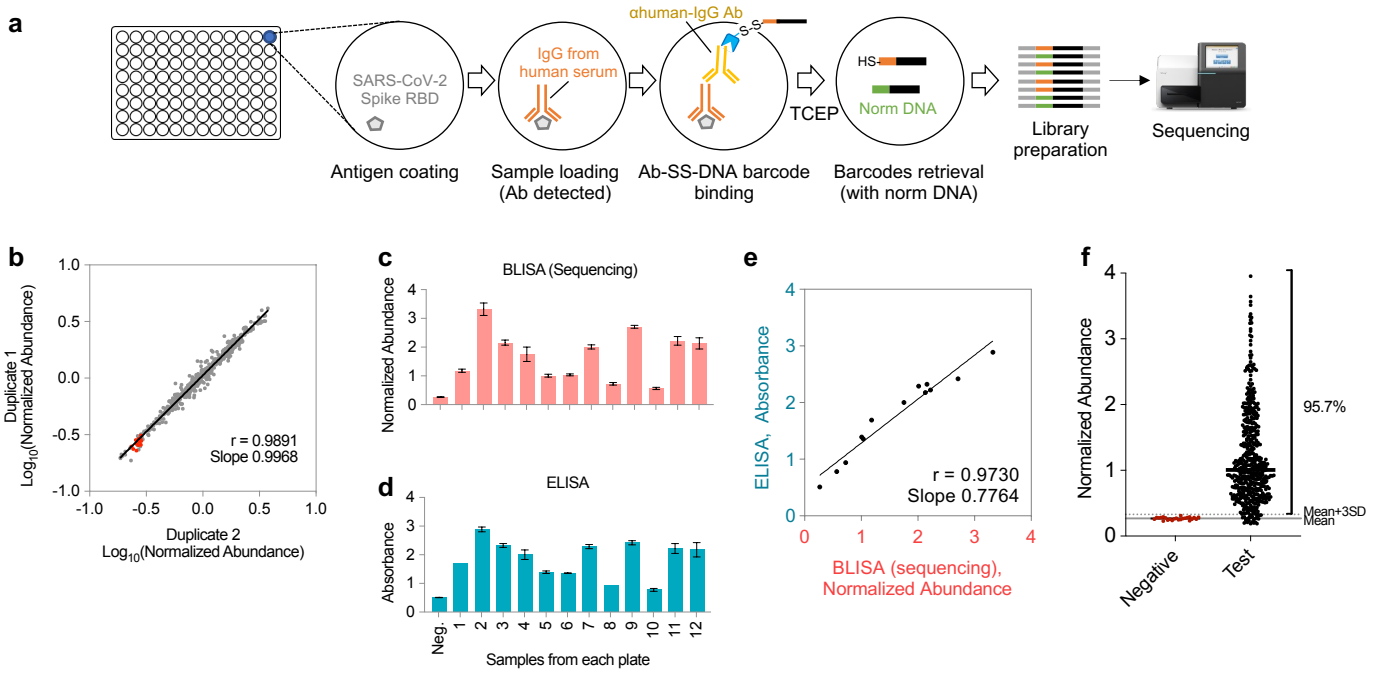

Fig. 5. HTS-based BLISA for high-throughput detection of IgGs in human serum samples. a, Workflow of sandwich immunoassay-based IgG detection using BLISA. **b**, Pearson's correlation between results from two technical duplicate. Red dots represent negative samples. **c**–**d**, Quantification of anti-RBD IgG levels in twelve samples from vaccinated donors using HTS-based BLISA (**c**) and ELISA (**d**). **f**, Pearson's correlation between BLISA and ELISA results shown in (**c**) and (**d**). n = 2 replicates; mean±s.e.m.. **f**, Distribution of normalized IgG abundance in negative and test samples (n = 493). Red dots represent negative samples. The solid grey line indicates the mean normalized abundance of negative samples. The dotted grey line represents the mean plus three standard deviations (mean+3SD).

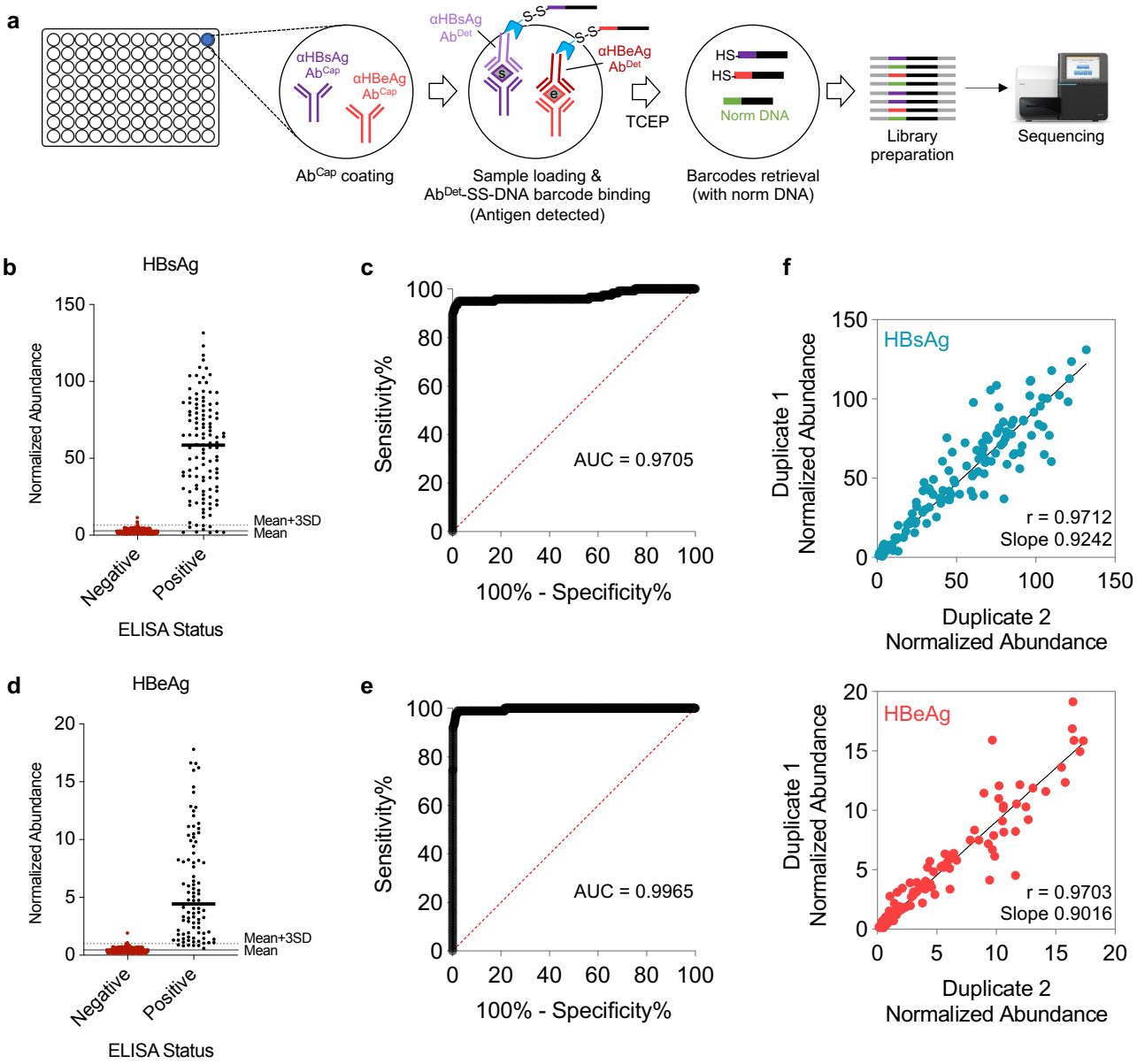

Fig. 6. HTS-based BLISA for high-throughput simultaneous detection of two HBV antigens in human serum samples. a, Workflow of sandwich immunoassay-based HBV antigen detection using BLISA. **b**–**c**, Sensitivity and specificity of two-plex BLISA for detecting HBsAg. *n*=462 ELISA-negative samples and 119 ELISA-positive samples from cohort 2. **d**–**e**, Sensitivity and specificity of two-plex BLISA on detecting HBeAg. *n*=505 ELISA-negative samples and 90 ELISA-positive samples from cohort 2. Solid grey lines indicate the mean normalized abundance of ELISA-confirmed negative samples. Dotted grey lines represent the mean+3 standard deviations (mean+3SD). **f**, Pearson's correlation between technical duplicates for HBsAg (upper) and HBeAg (bottom) measurements in serum samples from cohort 2 (*n*= 600).

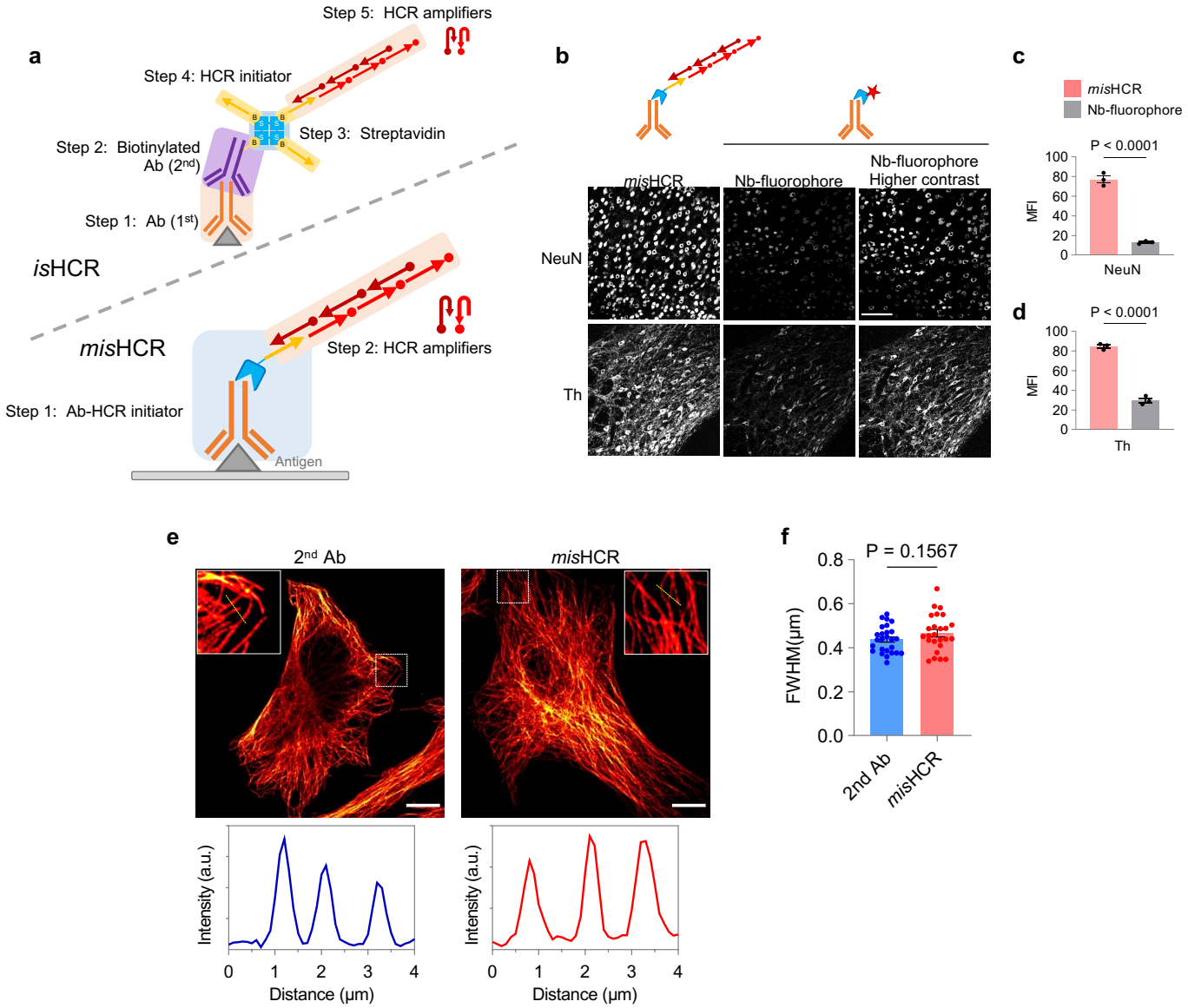

Extended Data Fig. 1. Characterization of *mis*HCR. a, Schematics of *is*HCR and *mis*HCR procedures. **b–d**, Fluorescence confocal images of mouse brain sections stained using *mis*HCR or conventional fluorescent immunohistochemistry with fluorophore-conjugated nanobodies. $n = 3$ brain sections for each group; mean±s.e.m.; two-sided unpaired *t*-test. Scale bar, 100 μm. **e**, Fluorescence confocal images of HeLa cells stained against α-tubulin using a conventional method with a fluorophore-conjugated secondary antibody (2nd Ab) (left) or *mis*HCR (right). Insets show zoomed-in views of the boxed region. Scale bar, 10 μm. Bottom panel shows representative intensity profiles along straight lines drawn perpendicular to microtubule structures. **f**, Quantification of full width at half maximum (FWHM) derived from intensity profiles along a straight line drawn perpendicular to microtubules structure stained using traditional immunohistochemistry (2nd Ab) or *mis*HCR. $n = 26$ for 2nd Ab and 25 for *mis*HCR; mean±s.e.m.; two-sided unpaired *t*-test.

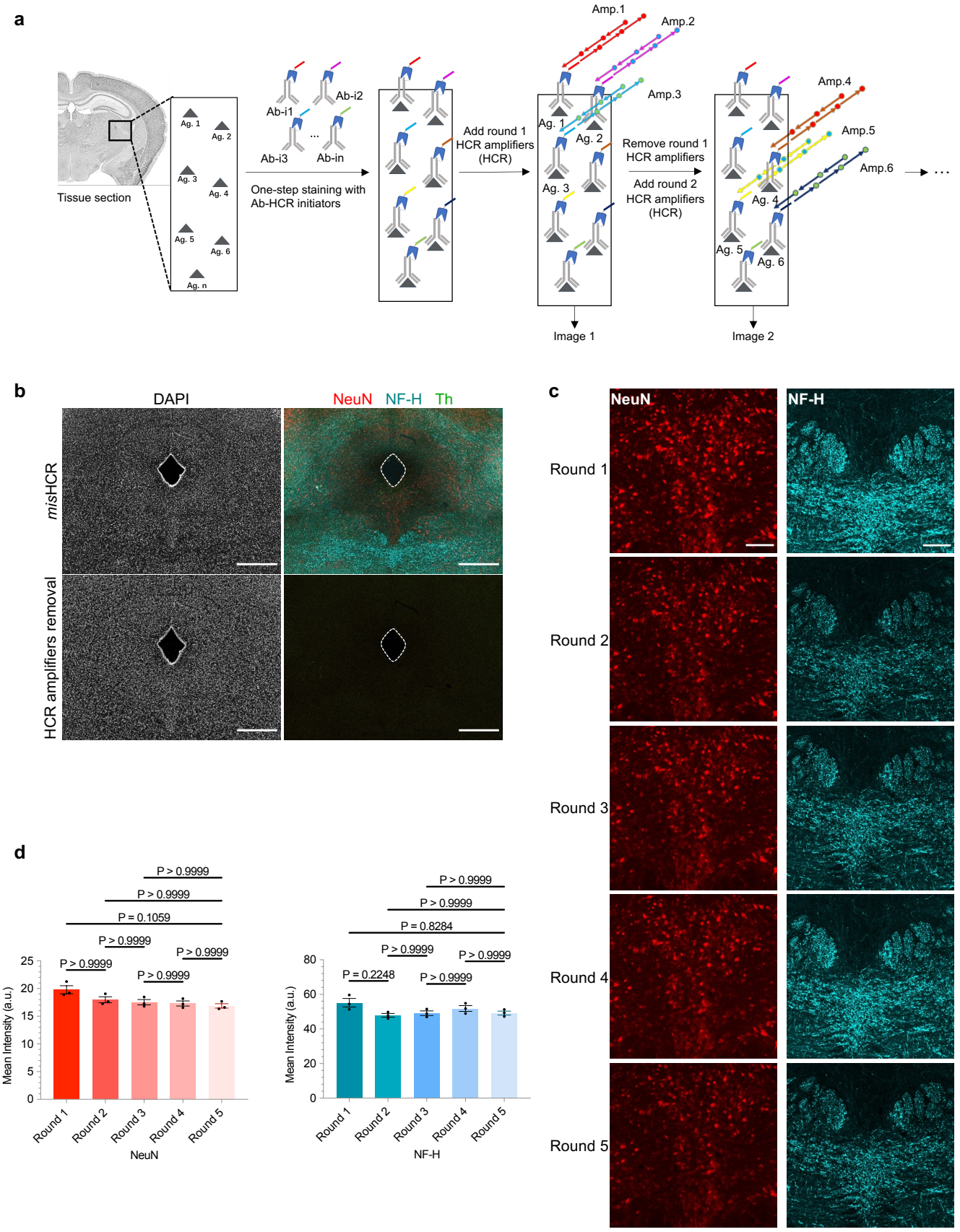

Extended Data Fig. 2. See next page for caption.

Extended Data Fig. 2. Efficient and reproducible HCR signal removal by formamide treatment. a, Workflow of *mis*HCR imaging. Pooled antibodies (Ab-i1 to Ab-in), each conjugated with distinct HCR initiators, are applied simultaneously for antigen (Ag. 1 to Ag. n) detection. Subsequently, sequential rounds of imaging are performed via hybridization and dehybridization of orthogonal HCR amplifier pairs (Amp.). **b**, Fluorescence confocal images of mouse brain sections before and after HCR amplifiers removal using formamide. Scale bar, 500 μm. **c**, Fluorescence confocal images of the DRN in mouse brain sections stained against NeuN and NF-H through five consecutive cycles of HCR amplification/formamide treatment. Scale bar, 100 μm. **d**, Quantification of mean fluorescence intensity for NeuN (left) and NF-H (right) after each round of HCR amplification. Images of each group were acquired using identical microscopy settings. n = 3 brain sections for each group; mean±s.e.m.; Dunn's multiple comparison tests.

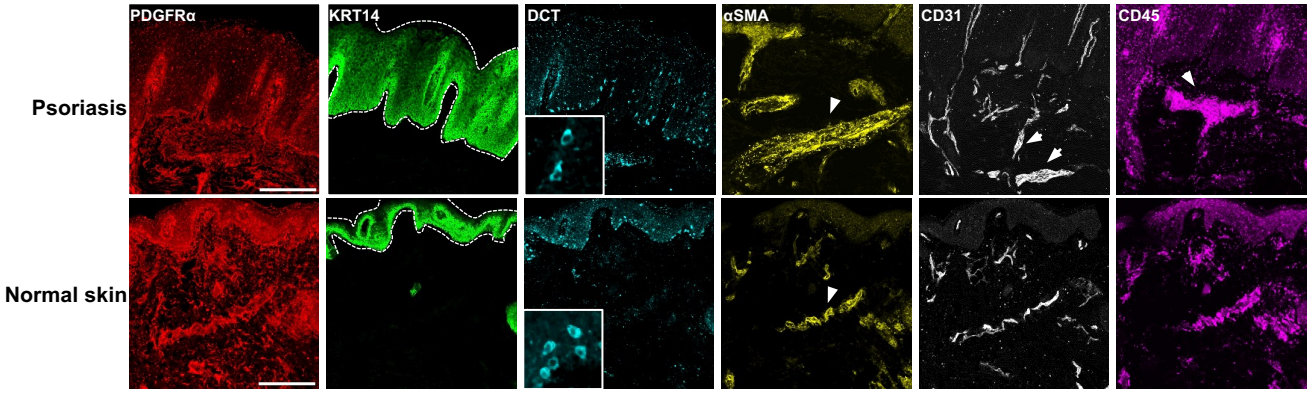

Extended Data Fig. 3. *Mis*HCR imaging of human psoriatic and healthy skin sections. Fluorescence confocal images of skin sections from a patient with psoriasis (up) and a healthy donor (bottom) stained against six antigens. The psoriatic skin sample corresponds to that shown in **Fig. 1d**. Dotted lines and arrows indicate pathological features characteristic of psoriatic skins. Scale bar, 300 μm.

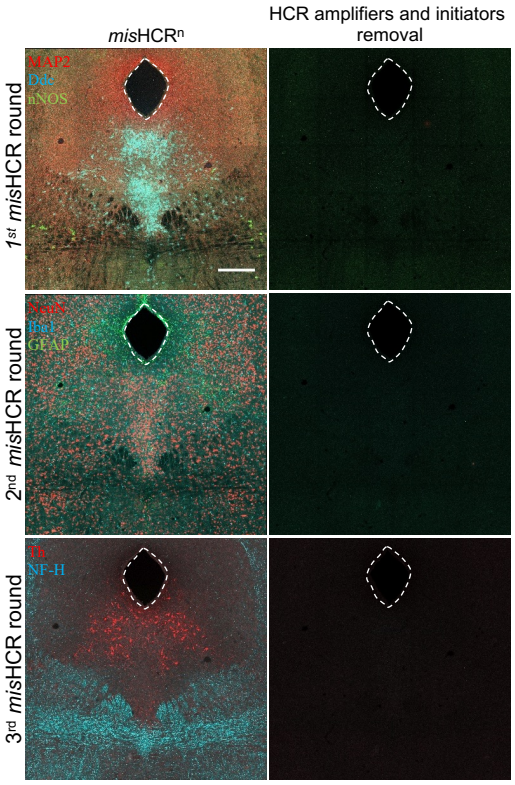

Extended Data Fig. 4. Efficient *mis*HCR signal removal by TECP treatment. Fluorescence confocal images of mouse brain sections before and after TCEP treatment to remove HCR amplifiers and initiators. The target molecules were MAP2, Ddc, and nNOS for the first round; NeuN, Iba1, and GFAP for the second round; Th, and NF-H for the third round. Scale bar, 300 μm. MAP2, microtubule-associated protein 2.

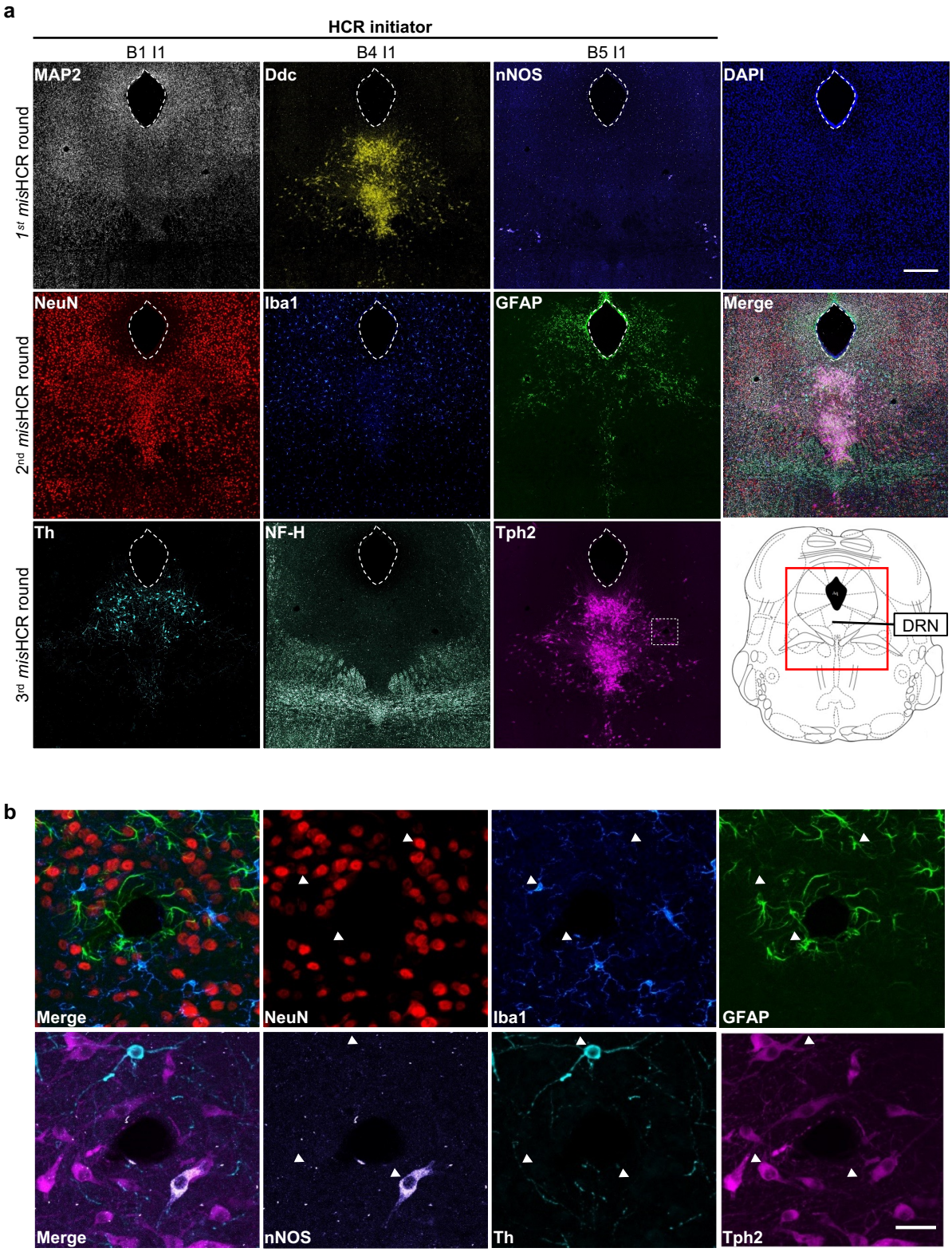

Extended Data Fig. 5. *mis*HCR^n for immunostaining nine target antigens using three orthogonal HCR initiators. a, Fluorescence confocal images of mouse brain sections stained against nine targets by three rounds of *mis*HCR. The red-boxed region of the mouse brain atlas shown in the bottom right indicates the imaging location. Scale bar, 300 μm. **b**, Zoomed-in views of the dotted-box region marked in **a**. Scale bar, 25 μm.

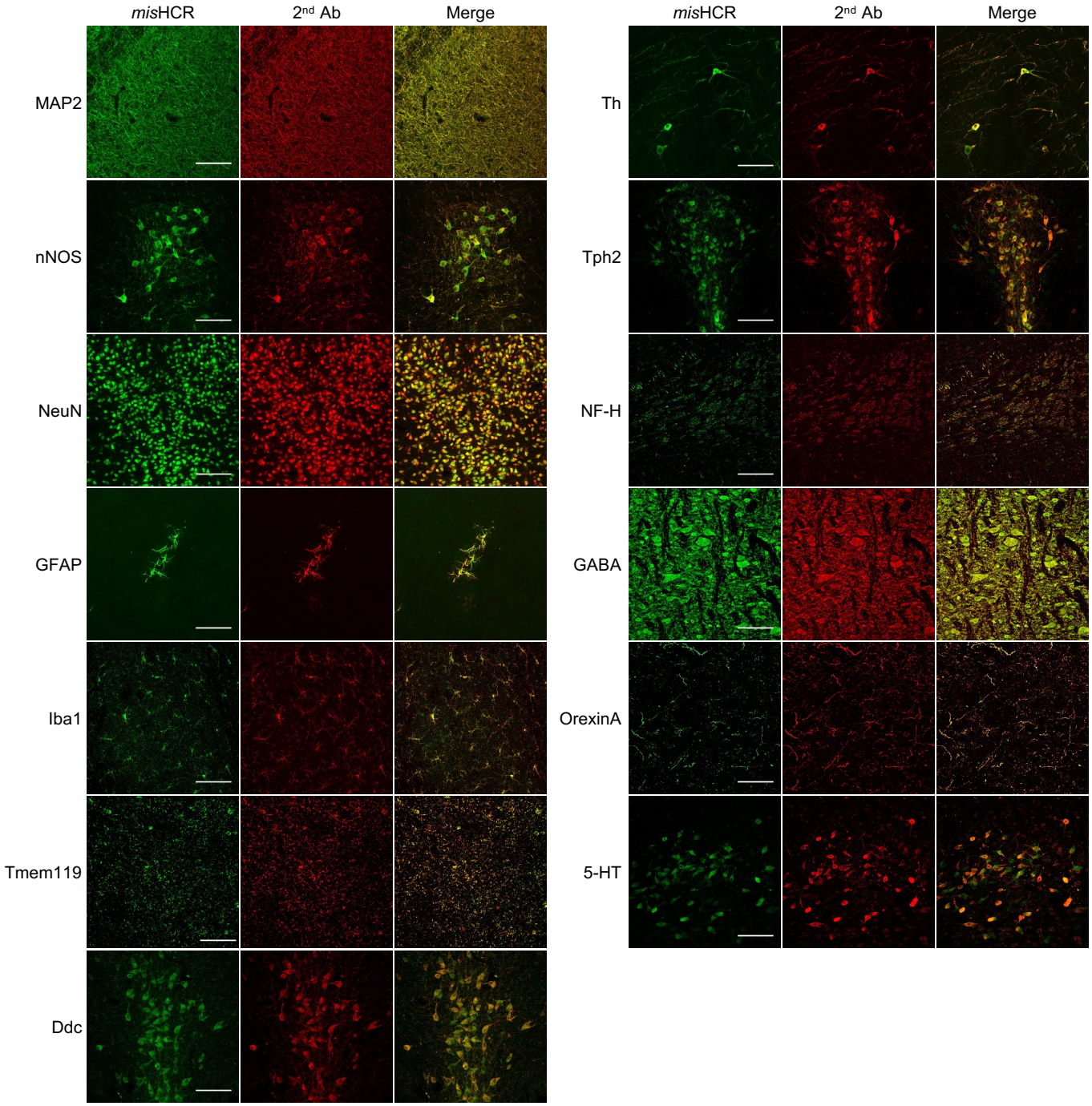

Extended Data Fig. 6. Validation of the specificity of *mis*HCR. Mouse brain sections were immunostained with primary antibodies against different antigens, followed by and simultaneous incubation with equal amounts of fluorophore-conjugated secondary antibodies (2nd Ab) and Nb-HCR initiators (*mis*HCR). Scale bar, 100 μm.

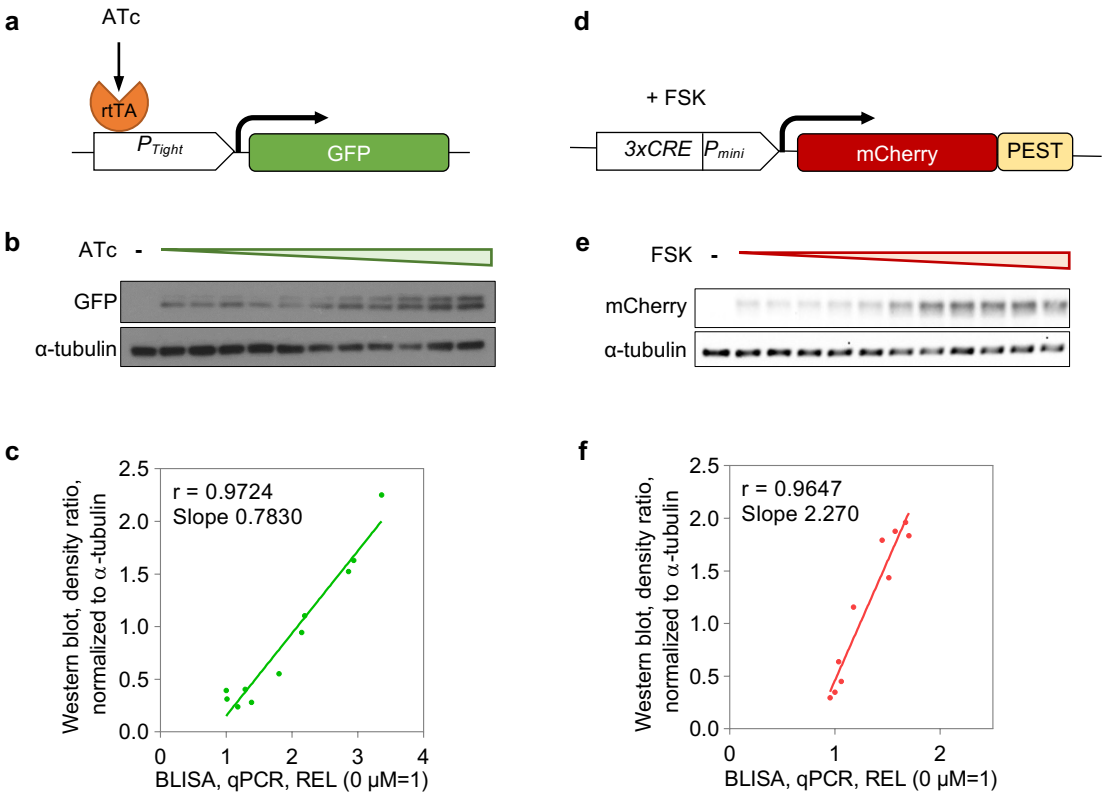

Extended Data Fig. 7. BLISA for detecting proteins endogenously expressed in cells. a, Schematics of the tetracycline-regulated gene expression system for driving GFP expression. **b**, Western blot of cell samples treated with varying concentrations of ATc. **c**, Pearson's correlations between qPCR-based BLISA and Western blot results for measuring relative expression level (REL, normalized to α-tubulin) of GFP. REL=$2^{-(CtGFP-Ct\alpha\text{-tubulin})}$. **d**, Schematics of the cAMP response element-mediated gene expression system for driving mCherry expression. **e**, Western blot of cell samples treated with varying concentrations of FSK. **f**, Pearson's correlations between qPCR-based BLISA and Western blot results for measuring REL (normalized to α-tubulin) of mCherry. REL=$2^{-(CtmCherry-Ct\alpha\text{-tubulin})}$.

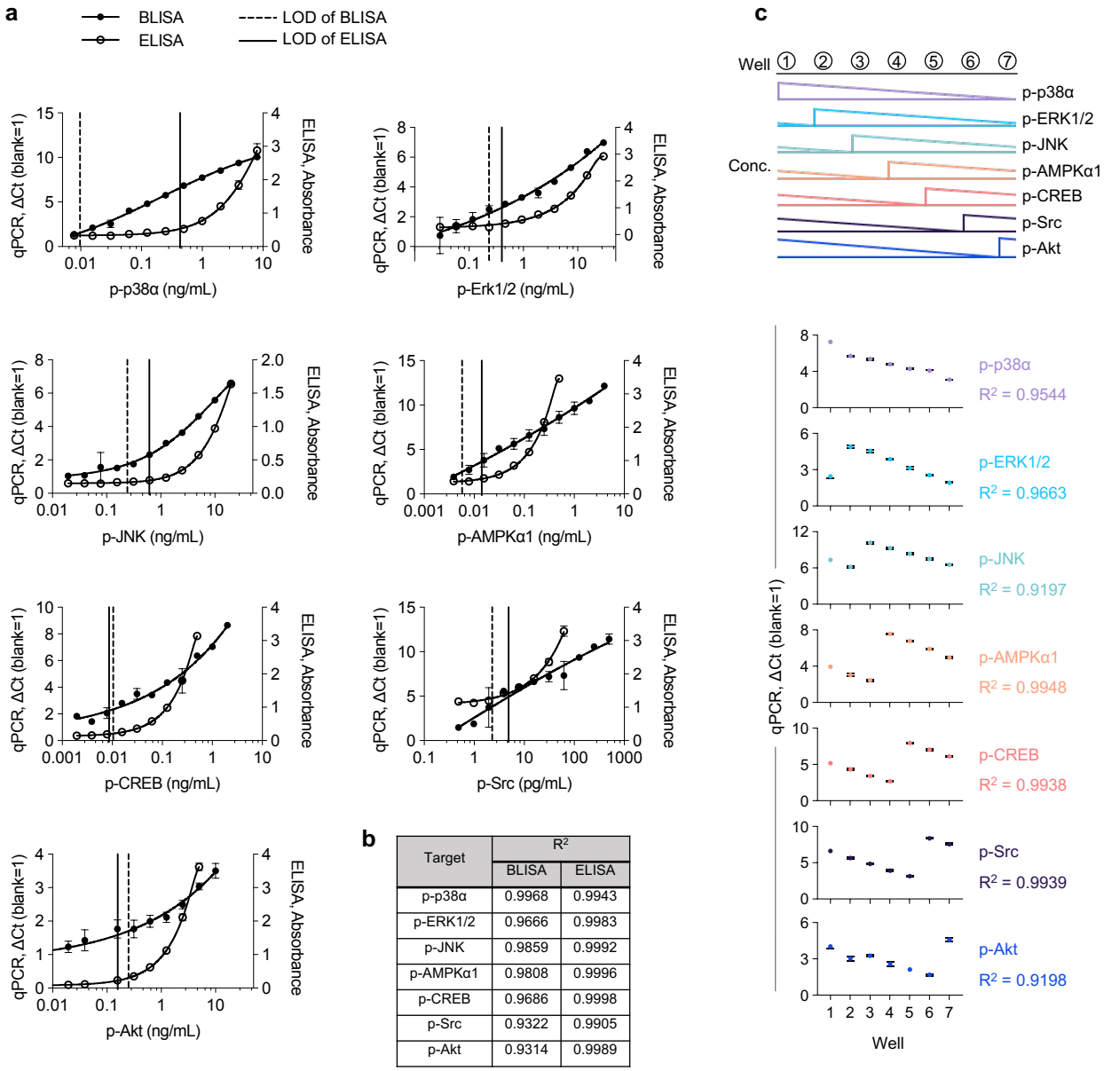

b

Target	R^2	
	BLISA	ELISA
p-p38α	0.9968	0.9943
p-ERK1/2	0.9666	0.9983
p-JNK	0.9859	0.9992
p-AMPKα1	0.9808	0.9996
p-CREB	0.9686	0.9998
p-Src	0.9322	0.9905
p-Akt	0.9314	0.9989

Extended Data Fig. 8. Comparative analysis of standard curves for magnetic bead-based BLISA and ELISA. a, Dose-response curves for seven purified phosphorylated proteins quantified using BLISA (qPCR, ΔCt) and ELISA (Absorbance). Curves were fitted using 4PL or 5PL functions. Limit of detection (LOD) was defined as the mean signal of the blank group plus three standard deviations. **b**, R^2 for the standard curves shown in panel **a**. **c**, Multiplexed detection of seven purified phosphorylated proteins using magnetic bead-based BLISA. n = 3 replicates; mean±s.e.m..

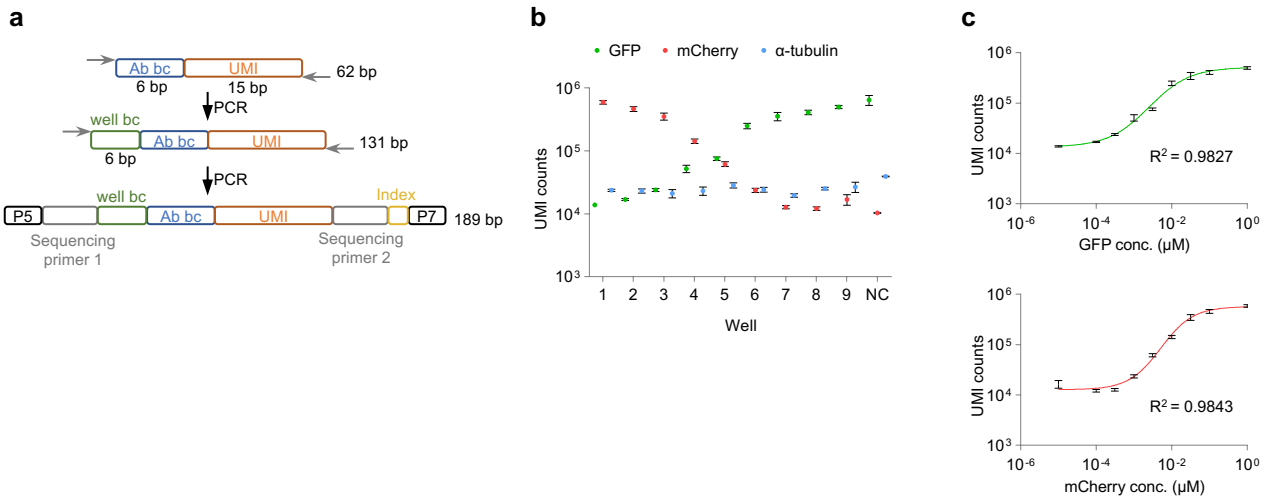

Extended Data Fig. 9. Validation of HTS-based BLISA. a, Schematics of DNA barcode design and amplicon generation for BLISA sequencing. Released DNA barcodes undergo a two-step PCR protocol for well barcode (well-bc) addition and Illumina sequencing adaptors tagging. **b**, UMI counts for three target proteinss (GFP, mCherry, and α-tubulin) in cell lysates spiked in with varying concentrations of GFP and mCherry. n = 3 replicates; mean±s.e.m.. **c**, Dose-response curves for the GFP (upper) and mCherry (bottom) fitted using a 5PL function. n=3 replicates; mean±s.e.m..

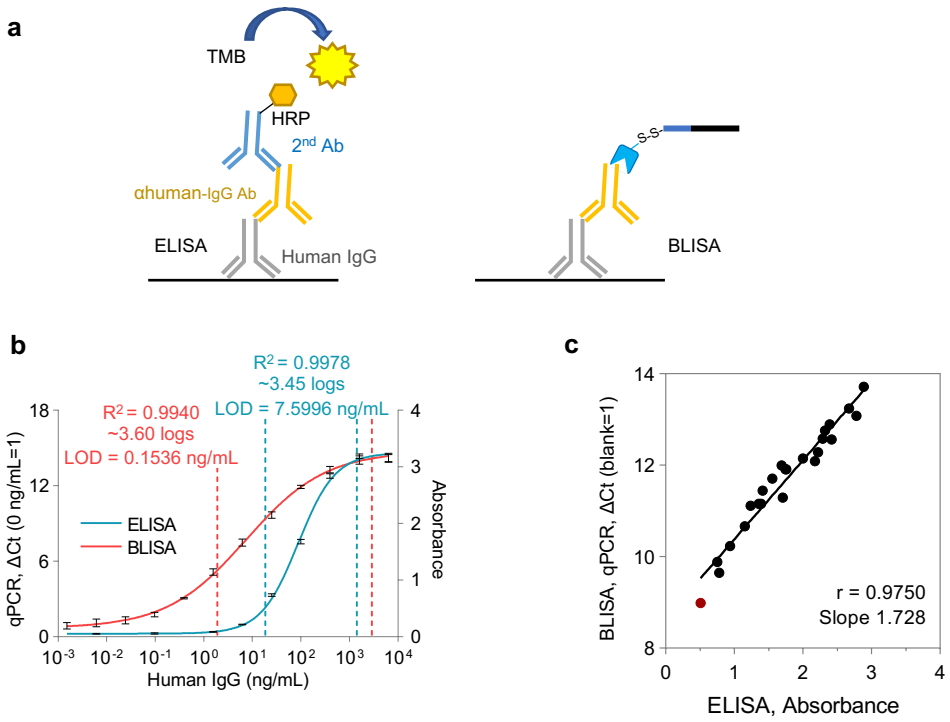

Extended Data Fig. 10. Comparative analysis of the sensitivity of BLISA and ELISA for human IgG detection. a, Schematics of ELISA (left) and BLISA (right) for human IgG detection. **b**, Dose-response curves for human IgG detection by BLISA and ELISA fitted using a 5PL function. The dynamic ranges of ELISA (blue) and BLISA (red) are indicated by dashed lines, spanning from the limit of quantification (LOQ) to the lower limit of 95% confidence interval. n = 3 replicates; mean±s.e.m.. **c**, Pearson's correlation between qPCR-based BLISA and ELISA results for anti-RBD IgG detection. The red dot represents the negative sample.

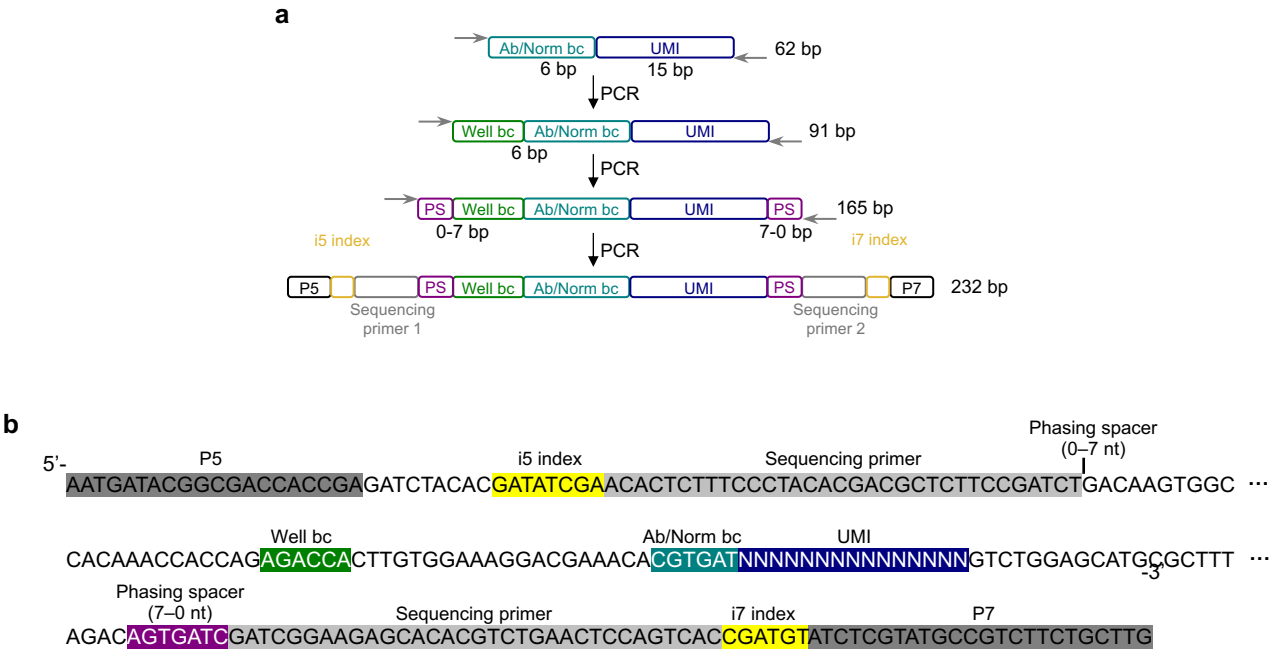

Extended Data Fig. 11. Sequencing library preparation for BLISA. a, Schematics of sequencing amplicon generation procedure. **b**, Annotated amplicon sequence of BLISA for Illumina sequencing.

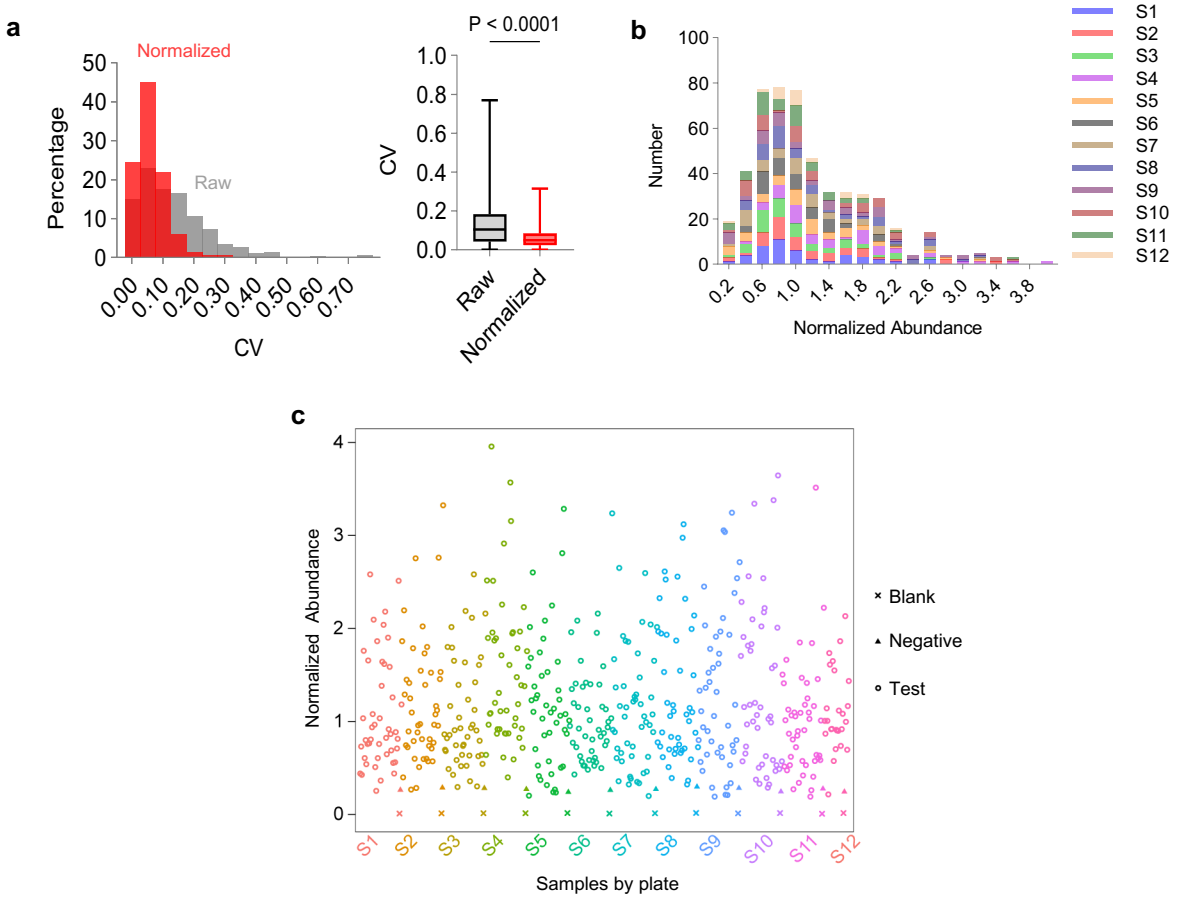

Extended Data Fig. 12. Quantification of anti-RBD IgG in human serum samples using HTS-based BLISA. a, Comparison of coefficient of variation (CV) between duplicates for raw (grey) and normalized (red) data. Histogram shows relative distributions of CV between duplicates. Box plots show median, interquartile range, and whiskers extending to the minimum and maximum. Two-sided paired t-test. **b**, Frequency distribution of normalized anti-RBD IgG abundances of test samples across assay plates. **c**, Scatter plot of normalized anti-RBD IgG abundances of individual serum samples (*n*=517) quantified using HTS-based BLISA. Each plate includes a negative control sample in duplicates.

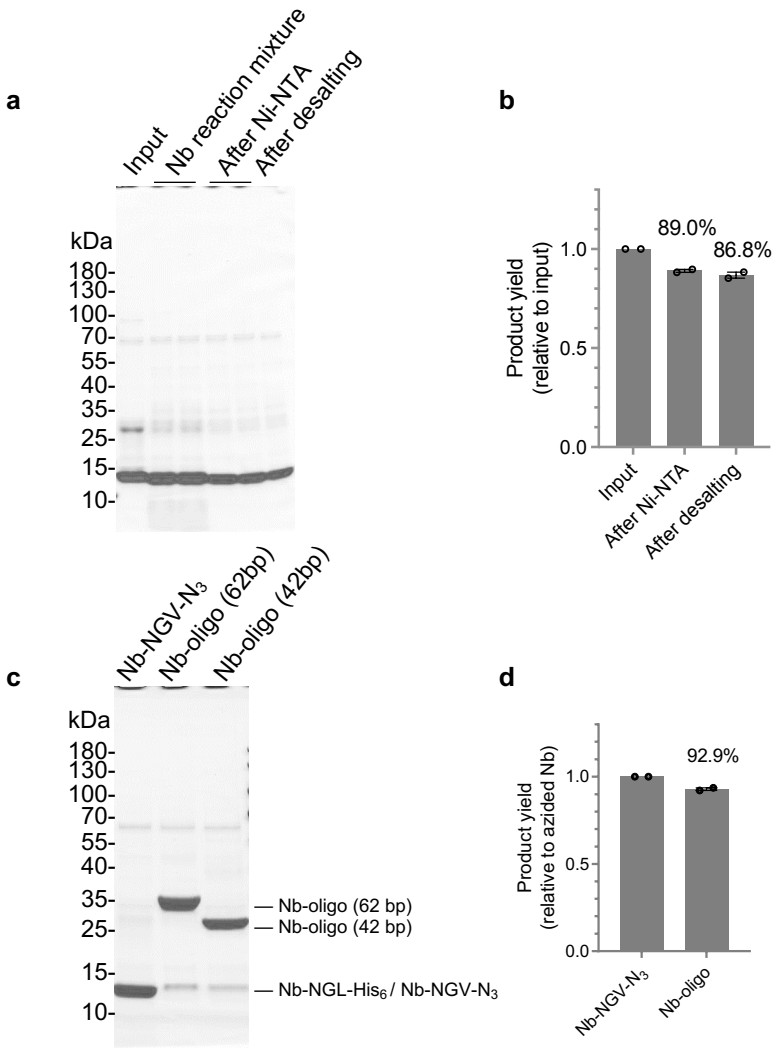

Supplementary Fig. 1. Efficiency assessment of nanobody-DNA oligo conjugation. a, Coomassie-stained reducing SDS-PAGE gel of protein products at each step of OaAEP1-mediated azide functional groups addition to nanobodies. The purified nanobody (*i.e.*, input) was incubated with OaAPE1 and azide-bearing substrate peptides (*i.e.*, Nb reaction mixture). After reaction, the products (*i.e.*, Nb-NGV-N_3) were purified by Ni-NTA agarose beads to remove unreacted His_6-tagged nanobody (*i.e.*, After Ni-NTA). The excess substrate peptides were further depleted using desalting columns (*i.e.*, After desalting). **b**, Quantification of OaAPE1-mediated reaction yields, determined by densitometric measurement of Nb-NGV-N_3 band intensities. **c**, Coomassie-stained reducing SDS-PAGE gel of Nb-NGV-N_3 and nanobodies conjugated with DNA oligo of different lengths (*i.e.*, Nb-oligo (62bp) and Nb-oligo (42bp)). **d**, Quantification of DNA conjugation yields, determined by densitometric measurement of band intensities corresponding to nanobody-DNA conjugates.

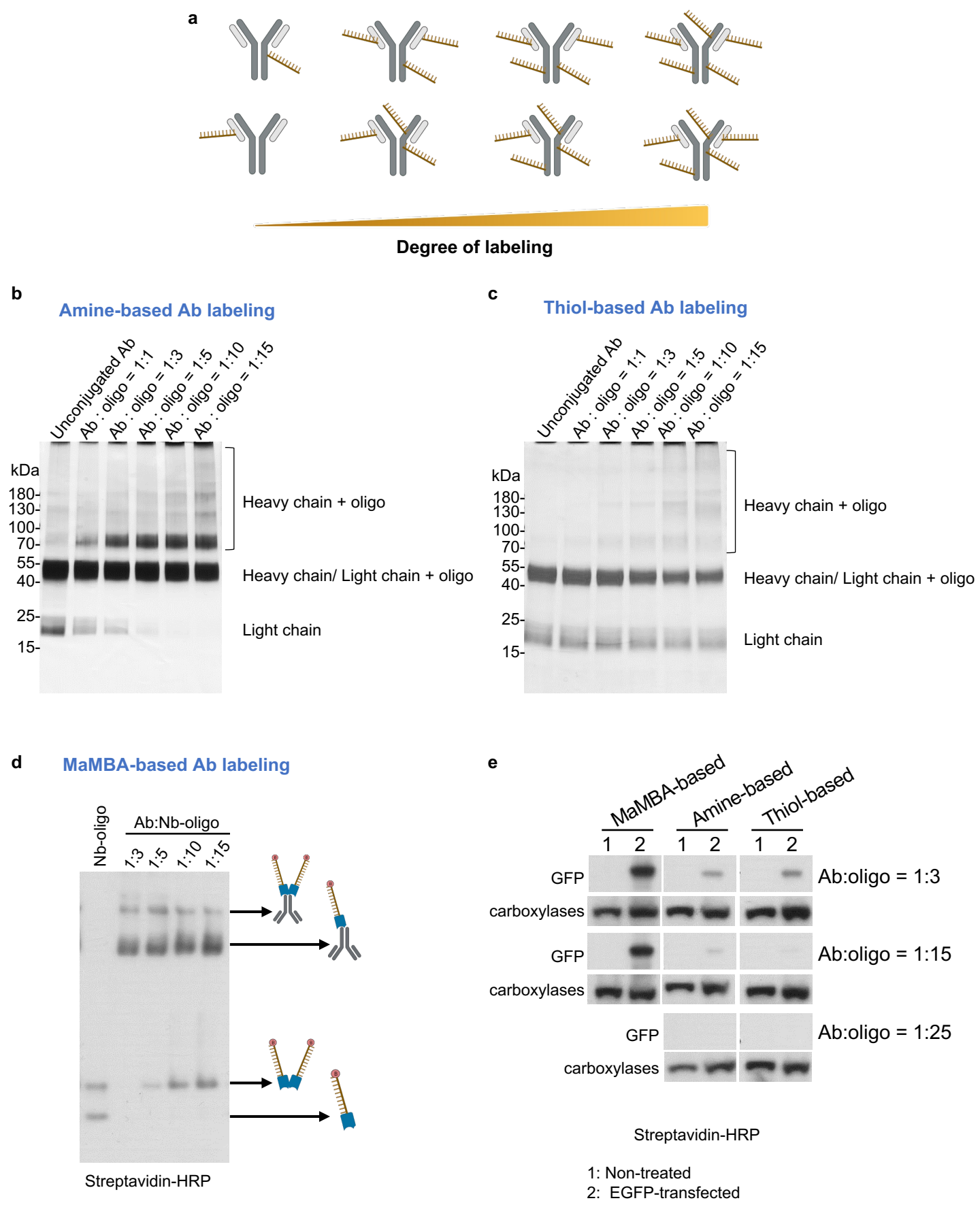

Supplementary Fig. 2. See next page for caption.

Supplementary Fig. 2. Comparison of antibody-DNA oligo labeling methods. a, Schematics of non-site-specific labeling methods for generating DNA oligo-conjugated antibodies with increased labeling degree. **b**, Silver-stained reducing SDS-PAGE gel of antibodies conjugated with 62bp DNA oligos using the amine-based method (Thunder-link antibody labeling kit) at various antibody:DNA ratios. **c**, Silver-stained reducing SDS-PAGE gel of antibodies conjugated with 62bp DNA oligos using the thiol-based method (thiol-maleimide reaction) at various antibody:DNA ratios. **d**, Western Blot of DNA oligo-labeled antibodies generated by MaMBA strategy using different antibody:nanobody-DNA oligo (Nb-oligo) ratios. Samples were separated by native PAGE and transferred to PVDF membrane for Western Blot. DNA oligos were 3'-biotin modified and detected using streptavidin. **e**, Western Blot of HEK 293T cell lysates with or without EGFP expression using different DNA oligo-labeled antibodies. The concentration of anti-GFP antibodies were identical for each group. DNA oligos were 3'-biotin modified and detected using streptavidin. All groups were chemiluminescently detected simultaneously. Endogenous biotinylated carboxylases in cell lysates served as loading controls.

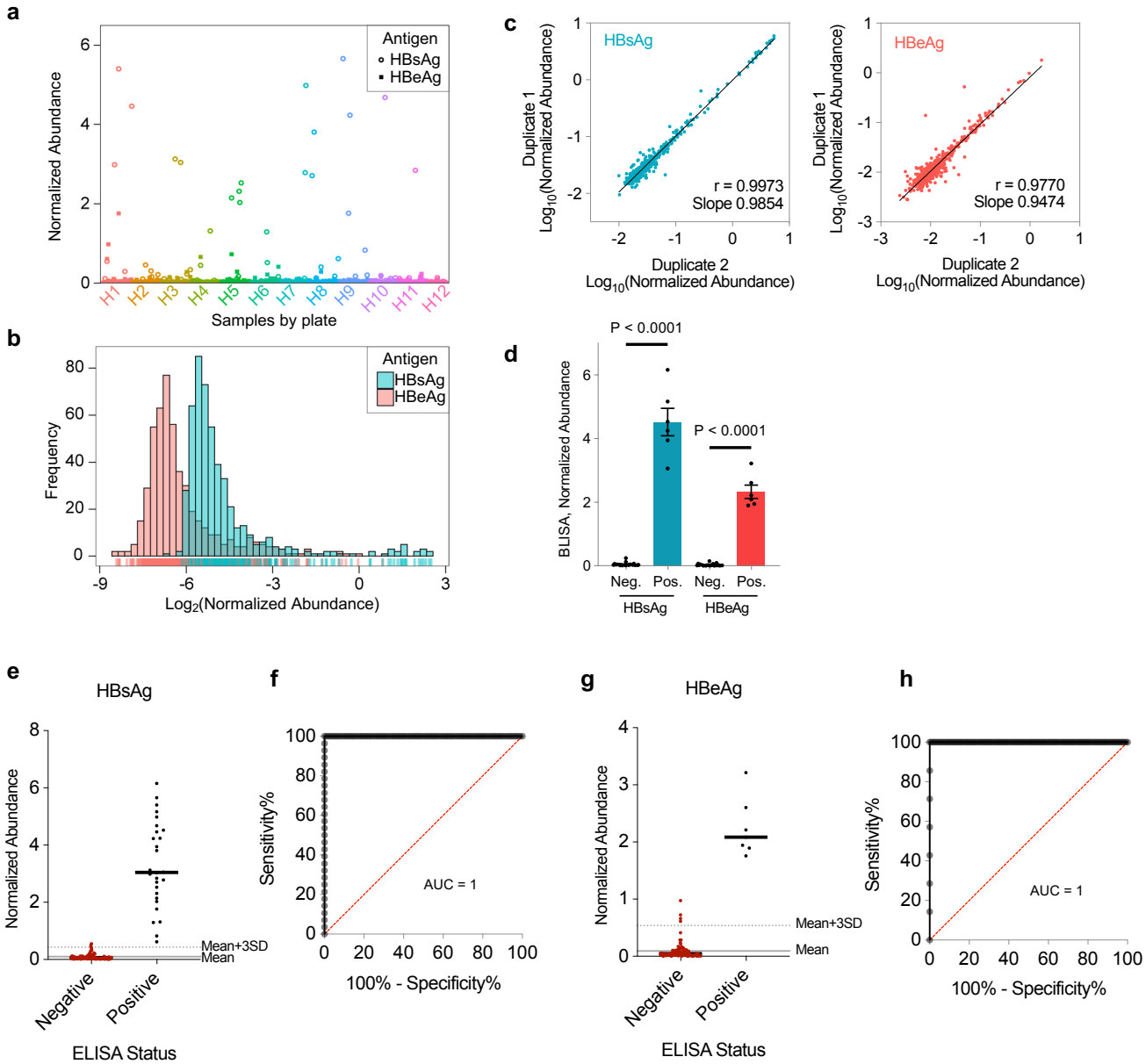

Supplementary Fig. 3. HTS-based BLISA for high-throughput detection of two HBV antigens in serum samples from cohort 1. a, Scatter plot of normalized HBsAg and HBeAg abundances of individual serum samples (*n*= 529) quantified using HTS-based 2-plex BLISA.. **b**, Frequency distributions of normalized a HBsAg (blue) and HBeAg (red) abundances of test samples. **c**, Pearson's correlation between technical duplicates for HBsAg (left) and HBeAg (right) measurements. **d**, HBsAg and HBeAg levels of control samples in cohort 1 measured by HTS-based BLISA. Histogram of normalized HBsAg and HBeAg abundances in negative ($HBsAg^{-}HBeAg^{-}$) and positive ($HBsAg^{+}HBeAg^{+}$) control groups were quantified using HTS-based BLISA. *n* = 25 for $HBsAg^{-}HBeAg^{-}$ and 6 for $HBsAg^{+}HBeAg^{+}$; mean±s.e.m.; Two-sided unpaired t-tests. **e**–**f**, Sensitivity and specificity of two-plex BLISA for detecting HBsAg. *n*=87 ELISA-negative samples and 28 ELISA-positive samples from cohort 1. **g**–**h**, Sensitivity and specificity of two-plex BLISA for detecting HBeAg. *n*=108 ELISA-negative samples and 7 ELISA-positive samples from cohort 1. Solid grey lines indicate the mean normalized abundance of ELISA-confirmed negative samples. Dotted grey lines represent the mean+3 standard deviations (mean+3SD).

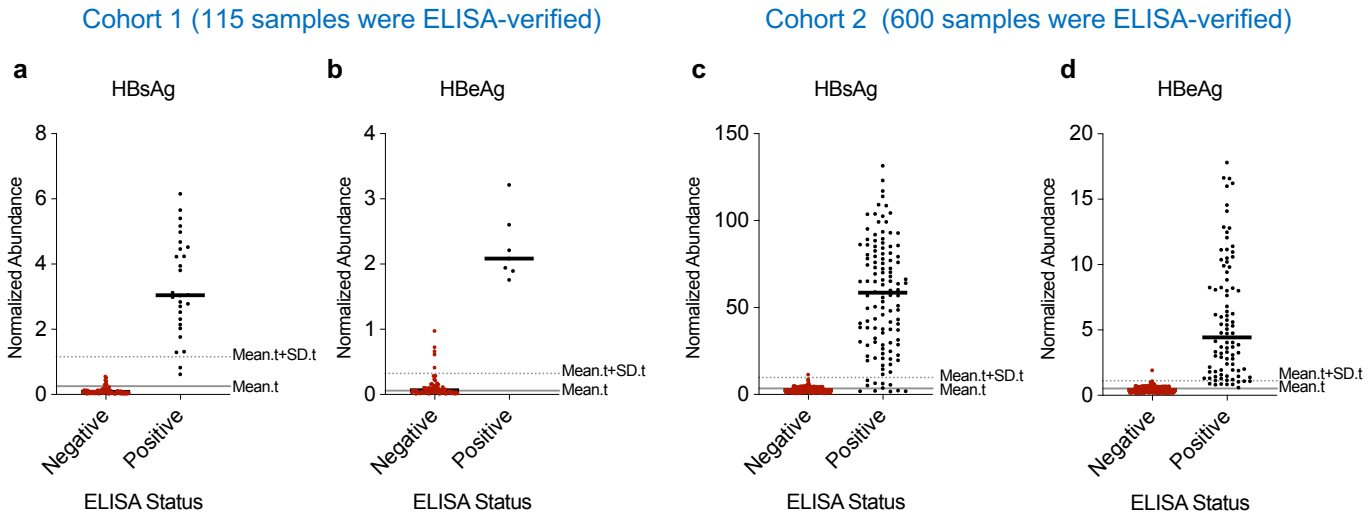

Supplementary Fig. 4. Performance evaluation of two-plex BLISA for detecting HBV antigens using ELISA-independent thresholds. a–b, Sensitivity and specificity of two-plex BLISA for detecting HBsAg (**a**) and HBeAg (**b**) in serum samples from cohort 1. Solid grey lines indicate the mean normalized abundance of test samples (mean.t; *n*=529). Dotted grey lines represent the mean+standard deviations (mean.t+SD.t). **c–d**, Sensitivity and specificity of two-plex BLISA for detecting HBsAg (**c**) and HBeAg (**d**) in serum samples from cohort 2. Solid grey lines indicate the mean normalized abundance of test samples (mean.t; *n*=500). Dotted grey lines represent the mean+standard deviations (mean.t+SD.t).

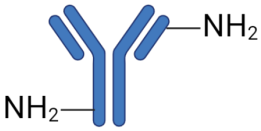

Amine-based Ab labeling			
Material preparation			Requirements[#]
Ab	Step 1	Buffer exchange	1 mg/mL concentration recommended
	Step 2	Activation	
	Step 3	Desalting	
Oligo	Step 1	Activation	Three to fifteen times of antibody amounts
	Step 2	Desalting	
Reaction			

Thiol-based Ab labeling			
Material preparation			Requirements[#]
Ab	Step 1	Buffer exchange	0.05 to 2 mg/mL concentration
	Step 2	Activation	
	Step 3	Desalting	
	Step 4	Desalting (2nd)	
Oligo	Step 1	Activation	Three to five times of antibody amounts
	Step 2	Desalting	
Reaction			

MaMBA-based Ab labeling		
Material preparation		Requirements
Ab	On-the-shelf	None
Nb-oligo	Prepared in batches and used on demand	Two times of antibody amounts recommended
Reaction		

[#]Requirements according to the manufacturer's instructions from commercial kit.

Supplementary Fig. 5. Comparison of the amine-based, thiol-based, and MaMBA-based antibody labeling methods.